

AD _____

Award Number: W81XWH-04-2-0022

TITLE: Ö^ç^|[] { ^} of Á ÄT ^ |ç^æÔ[||ä æ[Á[ÁU[{ } Äæää o@|æ ^

PRINCIPAL INVESTIGATOR: Y ÄÖää•Á &S^} } æÄT ÄÖÄU@ÖÈ

CONTRACTING ORGANIZATION: V@ÁW ä^|•æ Á ÁU^} } •^|çæ æ
Ú@æ^}] @ÄÖÄU@F@ Á

REPORT DATE: ÁR } ^ 2011

TYPE OF REPORT: O} ^ æ

PREPARED FOR: U.S. Army Medical Research and Materiel Command
Fort Detrick, Maryland 21702-5012

DISTRIBUTION STATEMENT: Approved for public release; distribution unlimited

The views, opinions and/or findings contained in this report are those of the author(s) and should not be construed as an official Department of the Army position, policy or decision unless so designated by other documentation.

REPORT DOCUMENTATION PAGE

Form Approved
OMB No. 0704-0188

Public reporting burden for this collection of information is estimated to average 1 hour per response, including the time for reviewing instructions, searching existing data sources, gathering and maintaining the data needed, and completing and reviewing this collection of information. Send comments regarding this burden estimate or any other aspect of this collection of information, including suggestions for reducing this burden to Department of Defense, Washington Headquarters Services, Directorate for Information Operations and Reports (0704-0188), 1215 Jefferson Davis Highway, Suite 1204, Arlington, VA 22202-4302. Respondents should be aware that notwithstanding any other provision of law, no person shall be subject to any penalty for failing to comply with a collection of information if it does not display a currently valid OMB control number. PLEASE DO NOT RETURN YOUR FORM TO THE ABOVE ADDRESS.

1. REPORT DATE (DD-MM-YYYY) 01-06-2011	2. REPORT TYPE Annual	3. DATES COVERED (From - To) 17 MAY 2010 - 16 MAY 2011		
4. TITLE AND SUBTITLE Development of a Multileaf Collimator for Proton Radiotherapy		5a. CONTRACT NUMBER		
		5b. GRANT NUMBER W81XWH-04-2-0022		
		5c. PROGRAM ELEMENT NUMBER		
6. AUTHOR(S) W. Gillies McKenna, M.D., Ph.D. E-Mail: tochner@uphs.upenn.edu		5d. PROJECT NUMBER		
		5e. TASK NUMBER		
		5f. WORK UNIT NUMBER		
7. PERFORMING ORGANIZATION NAME(S) AND ADDRESS(ES) The University of Pennsylvania Philadelphia, PA 19104		8. PERFORMING ORGANIZATION REPORT NUMBER		
9. SPONSORING / MONITORING AGENCY NAME(S) AND ADDRESS(ES) U.S. Army Medical Research and Materiel Command Fort Detrick, Maryland 21702-5012		10. SPONSOR/MONITOR'S ACRONYM(S)		
		11. SPONSOR/MONITOR'S REPORT NUMBER(S)		
12. DISTRIBUTION / AVAILABILITY STATEMENT Approved for Public Release; Distribution Unlimited				
13. SUPPLEMENTARY NOTES				
14. ABSTRACT This report describes the sixth year of a project to design and construct multileaf collimators (MLC) to be used in proton radiotherapy, the fifth year of the project to develop scanned beam technology for proton radiotherapy, and the fourth year of the project to develop image guided treatment protocols for proton therapy. This research project is a joint collaborative effort between the University of Pennsylvania (HUP) and the Walter Reed Army Medical Center (WRAMC), and is part of a larger project to build a state-of-the-art proton radiotherapy facility in Philadelphia. The accomplishments during the past year of the project are described in this report.				
15. SUBJECT TERMS Radiation Oncology, Proton Therapy, Multileaf Collimator, MLC, Conformal Radiotherapy				
16. SECURITY CLASSIFICATION OF: a. REPORT U		17. LIMITATION OF ABSTRACT UU	18. NUMBER OF PAGES 54	19a. NAME OF RESPONSIBLE PERSON USAMRMC A 19b. TELEPHONE NUMBER (include area code)
b. ABSTRACT U		c. THIS PAGE U		

Table of Contents

Introduction	4
Body	5
Key Research Accomplishments.....	53
Reportable Outcomes.....	53
Conclusions.....	53

Introduction

The overall goal of this multi-year research project in collaboration with the Walter Reed Army Medical Center is to develop the necessary technology to make the proton facility that is being constructed in Philadelphia the most advanced proton radiotherapy center. The first technology is the development of a multileaf collimator (MLC) for proton therapy and investigates the issues that must be resolved to use an MLC in proton therapy. The second technology under study is the optimization of the spot-scanning delivery technique including the effects of organ motion. The third technology is the development of protocols to apply the techniques of image-guided and adaptive radiotherapy to proton therapy, and to develop a decision-making algorithm to maximize the efficiency of the facility. This report describes the progress during the sixth year of the expected seven-year process. Included in that progress are the following activities and achievements: (1) Use of the GEANT4 Monte Carlo code, which was developed in the previous years of the project, to test various MLC designs, culminating in the delivery of the first MLC and the status of the on-going tests of that MLC; (2) Use of the same simulation program to optimize the dose distribution from scanned beams accounting for inhomogeneities and organ motion; and (3) Development of treatment protocols and an understanding of the factors that are involved to efficiently utilize the beam.

Body

In June 2006, following years of defining specifications and evaluating proposals, the University of Pennsylvania Health System (UPHS) signed a contract with Ion Beam Applications, S.A. (IBA). In addition to the details associated with the delivery of a proton therapy system the contract included three development agreements directly related to the work supported by this grant to develop technology for proton therapy. The development agreements between UPHS, IBA and Varian Medical Systems, Inc. (the leading conventional radiotherapy vendor) were: (1) to develop a multileaf collimator for the IBA proton delivery system, (2) to develop a cone-beam CT to permit imaging of the patient in the treatment room, and (3) to develop the pencil-beam scanning algorithm of the Varian treatment planning system.

Much of the effort in the past year has been to: (1) test the prototype MLC and then install and test the final MLC; (2) design a system that permits the treatment of shallow targets with scanned beams; and (3) write treatment protocols and submit them to regulatory bodies for approval. To that end UPHS personnel have met with IBA and Varian engineers multiple times and have teleconferences or WebEx-type remote meetings nearly every week. The MLC, which has the highest priority because the treatment rooms cannot be commissioned without it, is the most advanced of these projects. The scanning development is close to completion; the clinical implementation had been delayed by approximately one year because we did not feel that the IBA system was mature enough for routine clinical use. The cone-beam CT development has made the least progress thus far, but we continue to work with several vendors and other proton facilities to find an affordable solution. Cone-beam CT technology has only recently been introduced to conventional radiotherapy and is constantly being upgraded. Our challenge is to design a device that will be able to easily follow the advances the system makes in conventional therapy.

This report concentrates on the sixth year achievements of the multileaf collimator development, the fifth year of work on the spot-scanning/motion project, and the fourth year on the development of image-guided and adaptive radiotherapy protocols. The Statement of Work in the approved grant proposals included the following items to be investigated. (Note: to minimize confusion, the years in which we expected to perform the work have been replaced by the fiscal year because there are three separate starting dates.) Because of the delay in choosing the vendor several of the aims that were originally planned to be completed by now, especially related to the design and prototyping of the MLC system, are still ongoing. The current schedule is such that the fifth treatment room (Proton 2 with pencil beam scanning) will be commissioned in late 2011. The items in the Statement of Work are listed below with a comment on the status of any item that was to have work performed by this time.

The projects identified included:

1. Multileaf collimator (MLC) for use on proton therapy gantries
2. Cone Beam CT (CBCT) on the proton gantry for localization of target volumes
3. Proton Radiography to determine dose and stopping power of various tissues
4. Positron Emission Tomography (PET) imaging on the gantry to evaluate dose deposition within tissues irradiated

5. Pencil Beam Scanning (PBS) proton beam using adaptive radiotherapy techniques based on implementation of MLC, Cone Beam CT, and PET imaging

Phase One- All the action items in the SOW for phase one were completed by us with minimal adjustments in some of the items that were required by the development of the proton system.

Phase Two- The SOW for phase two included mostly the development and implementation of Pencil Beam Scanning, and development of joint military UPENN telemedicine system. The delivery and installation of clinical PBS system by our contractor- IBA- has been delayed by IBA. The first PBS system is currently being installed and tested at our facility by IBA. All the action items in the SOW that are related to our preparation for PBS and could be done at the current stage of installation have been done. The telemedicine system with WRMC is working. We expect to have our first clinical PBS system before the end of the year and then will be able to complete the action items that are in the SOW of this phase.

Phase Three- The SOW included studying of imaging modalities for proton, development of CBCT, studying and development of adaptive proton therapy which is based on repeated imaging during proton therapy and development of smart scheduling system.

The studies of imaging modalities per the SOW were done.

We currently do not have CBCT despite intensive work and research to develop one. We are actively reviewing new idea to develop CBCT with IBA and have successfully completed preliminary testing. In this proposal the CBCT will be installed on the gantry. We plan to continue and develop this idea with IBA.

To satisfy the SOW regarding adaptive radiotherapy for proton we have developed IRB approved protocol which is currently being reviewed by the DOD. Once approved we will recruit the additional personal needed to execute it.

Current and near future plan to complete the SOW:

Complete the items that are related to PBS after the expected installation of PBS during the second quarter of 2012, as was detailed above.

We continue to review the new proposal for cone beam CT and we are expecting to proceed with the development of cone beam CT during the first half of FY2012.

Once final DOD approval is received we will continue the development of adaptive radiotherapy methodology which will continue until September of 2012.

We continue to develop the smart scheduling system as the department grows and plan to complete it by September of 2012

Progress

The work over the last year can be classified into three areas relating to progresses in: (A) MLC development, (B) spot-scanning development, and (C) protocol development.

A. MLC progress

I. Small field measurements

In our previous report, we compared simulation results with small field measurements for a pristine peak with a range of 24.67 cm using circular MLC shapes with several different diameters. The measurements were taken with a PPC05 ion chamber and the depth dose curves from simulation were found by integrating through a $1 \times 1 \text{ cm}^2$ square in the center of the water tank. We also made comparisons with measurements and Eclipse calculations of SOBPs with a range of 17.5 cm and a 10 cm modulation for a number of circular MLC shapes differing in diameter. The measured SOBP for a 1.8 cm diameter circular field size differed significantly from the Eclipse-calculated SOBP for the same field size. Measurements showed a larger decrease in dose for the small field size in comparison with the SOBPs for larger field sizes, although both Eclipse and measurement showed that the SOBP for the 1.8 cm diameter circular field had a significant downward slope in comparison with the SOBPs for larger field sizes. We found that as we decreased the area of the center of the water phantom through which the simulation is integrated below $1 \times 1 \text{ cm}^2$, the simulated SOBP deviated from the chamber-measured SOBP and approached the Eclipse-calculated SOBP.

In order to better understand the tilt in the SOBP for small field sizes, we looked at x- and y-profiles and XY-dose distributions at multiple depths for the 1.8 cm diameter circular field and the 5 cm diameter field (for comparison). The downward tilt implies that the long range protons are not depositing dose along the central axis, so we want to look at where they are traveling. Figure I.1 contains one of the SOBP comparisons described above from the last report containing measured and Eclipse-calculated SOBPs for various field sizes with the simulated SOBPs found using a $6 \times 6 \text{ mm}^2$ integration area through the center of the water phantom. Figure I.2 contains the XZ and YZ, 2D projections of the dose through the phantom which have been integrated through the y- and x-direction, respectively. The XY-dose distributions and profiles at different depths for the beams from Figure I.1 are shown in Figure I.3. The XY-dose distributions have a $6 \times 6 \text{ mm}^2$ square in black in the center to give an idea of the area being integrated through the z-direction to produce the simulated depth dose curves. The 1D profiles in the y-direction have the Eclipse-calculated y-profile at isocenter ($d = 12.5 \text{ cm}$) plotted for comparison of shape.

In addition to these small field measurements, we simulated a 9.55 cm range pristine peak with 0.86 cm side square field size for which measurements had been taken with a PPC05 ion chamber and an SFD stereotactic diode. The chamber and diode measurements differed by approximately 20% in entrance dose, with the chamber dose being lower than the diode. The measured peaks were plotted with the simulated pristine peak obtained using $12 \times 12 \text{ mm}^2$, $10 \times 10 \text{ mm}^2$, $8 \times 8 \text{ mm}^2$, $6 \times 6 \text{ mm}^2$, and $4 \times 4 \text{ mm}^2$ integration areas through the center of the water phantom. We found that the simulated peak matched with the chamber measurement when using an integration area of $12 \times 12 \text{ mm}^2$ through the center of the water phantom (which is a greater area than the field size), and that after shrinking the integration area to $4 \times 4 \text{ mm}^2$, the simulation entrance dose matched with that of the pristine peak measured using a diode. Although using an integration area smaller than

$4 \times 4 \text{ mm}^2$ was attempted, the data was too noisy and would require smaller voxels to be used in the phantom to get useful statistics. The voxels that were used in this simulation were $0.5 \times 0.5 \times 1.0 \text{ mm}^3$ in a $20 \times 20 \times 40 \text{ cm}^3$ water phantom. The results can be seen in Figure I.4 which shows the peaks measured with the chamber and diode as well as the simulated peak as a function of integration area through the center of the water tank. This shows that the chamber may not produce accurate measurements for small field sizes.

B6 range = 17.5cm, modulation = 10cm, 0.6cm integration

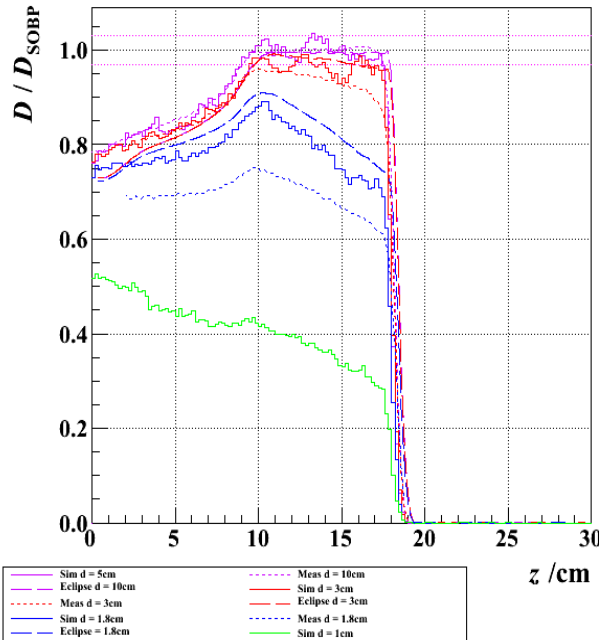


Figure AI.1: A comparison between SOBPs for multiple circular field sizes measured in a water tank with a PPC05 chamber (dotted lines), calculated in Eclipse (dashed lines), and simulated in a water phantom (solid lines). The SOBPs have a range of 17.5 cm and a modulation of 10 cm and were measured for circular field sizes with 10 (purple), 3 (blue), and 1.8 (blue) cm diameters and simulated using circular field sizes of 5, 3, 1.8, and 1 cm diameters. There is no noticeable difference for field sizes with diameters greater than 5 cm, so the simulation with 5 cm diameter field size corresponds with the measured SOBP for a 10 cm diameter field size. The SOBPs from the simulations have been obtained by integrating the dose over a $6 \times 6 \text{ mm}^2$ square through the center of the water phantom.

I.

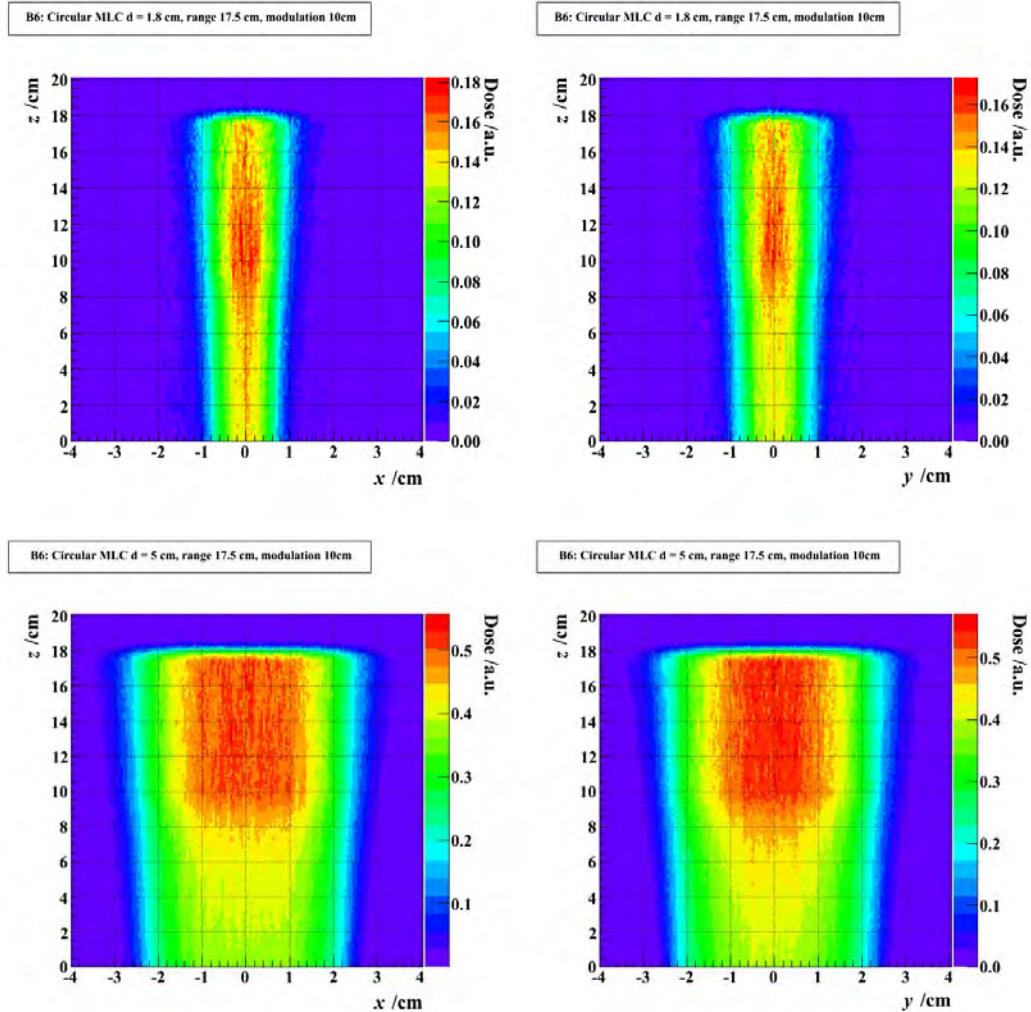
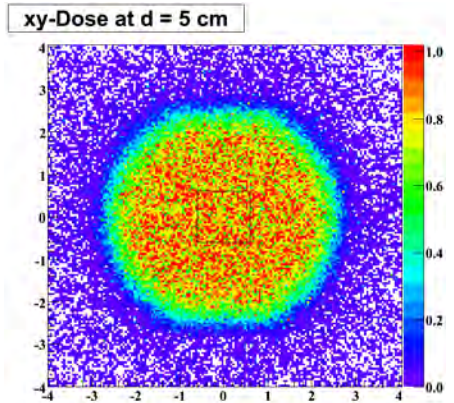
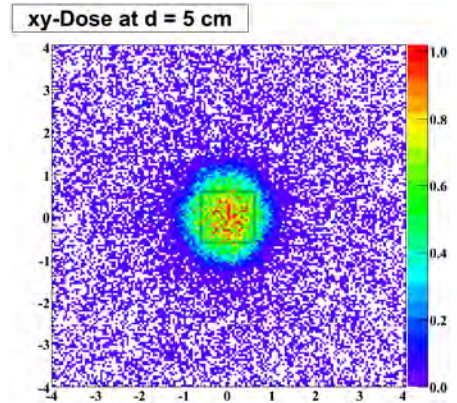
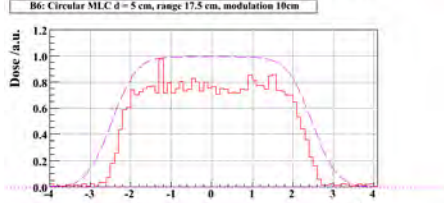
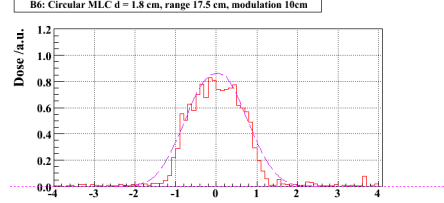
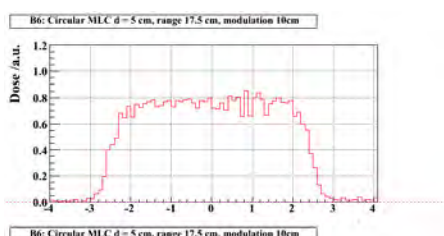
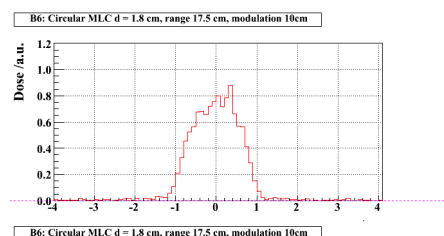
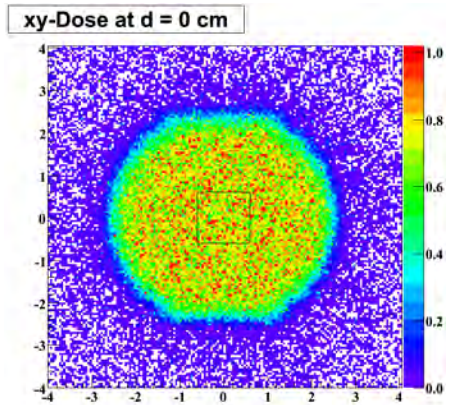
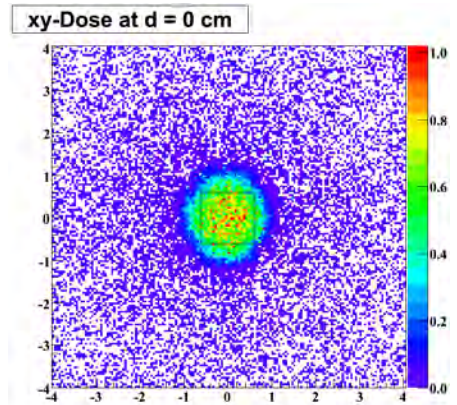
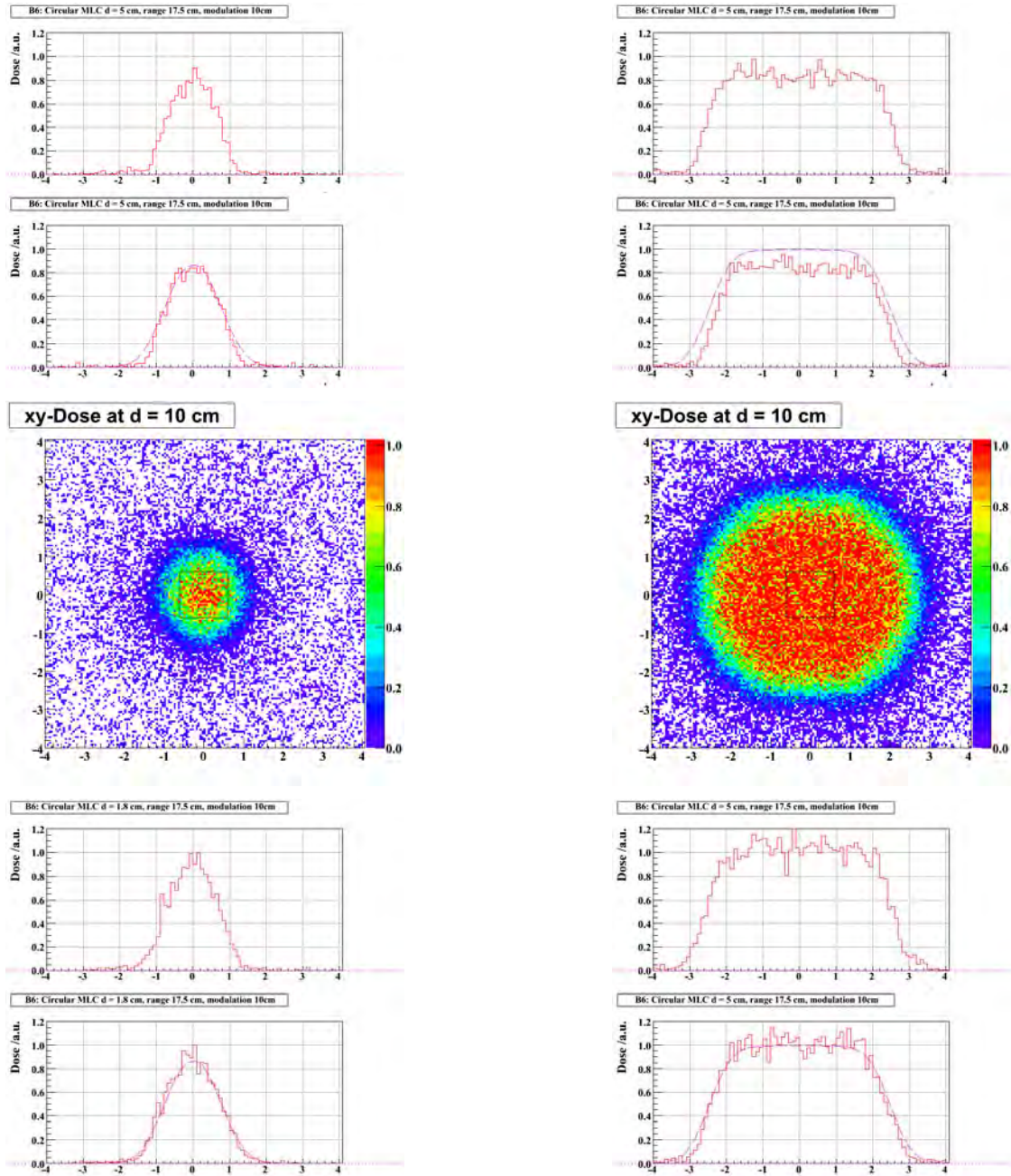
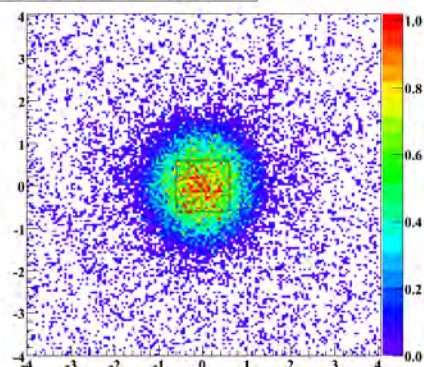


Figure AI.2: 2-Dimensional dose distributions for an SOBP with a range of 17.5 cm, modulation of 10 cm, and circular field sizes with a 1.8 cm (top) and 5 cm (bottom) diameter. The XZ-projections (left) have been integrated through the y-direction and the YZ-projections (right) have been integrated through the x-direction. They have been normalized to the dose in the center of the SOBP and the dose has been integrated through the entire phantom in the respective directions. They give a qualitative idea of where the long range protons are traveling for the small field in comparison with the larger field.

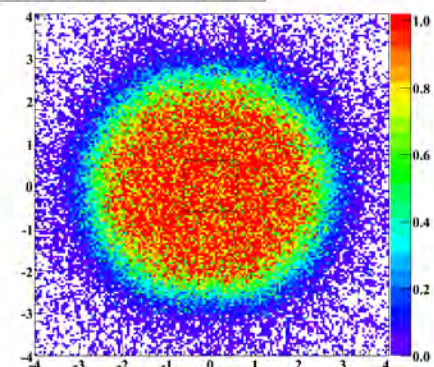




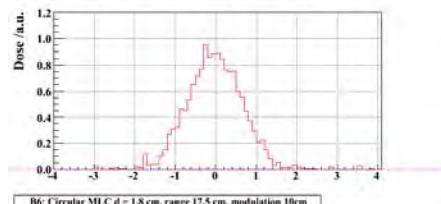
xy-Dose at $d = 12.5$ cm



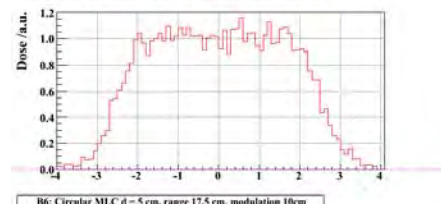
xy-Dose at $d = 12.5$ cm



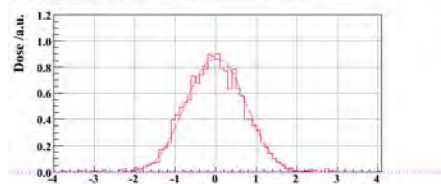
B6: Circular MLC $d = 1.8$ cm, range 17.5 cm, modulation 10cm



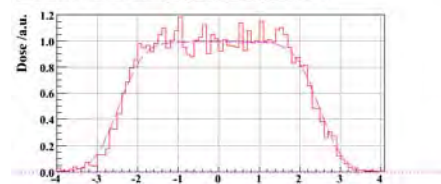
B6: Circular MLC $d = 5$ cm, range 17.5 cm, modulation 10cm



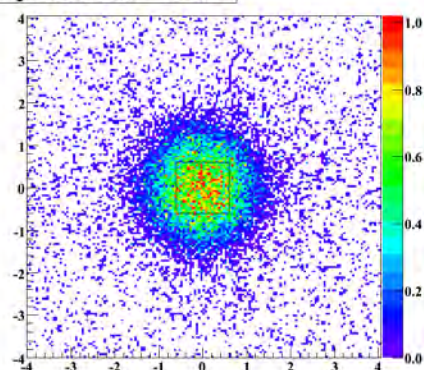
B6: Circular MLC $d = 1.8$ cm, range 17.5 cm, modulation 10cm



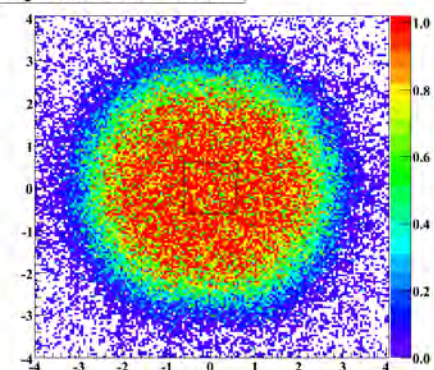
B6: Circular MLC $d = 5$ cm, range 17.5 cm, modulation 10cm



xy-Dose at $d = 15$ cm



xy-Dose at $d = 15$ cm



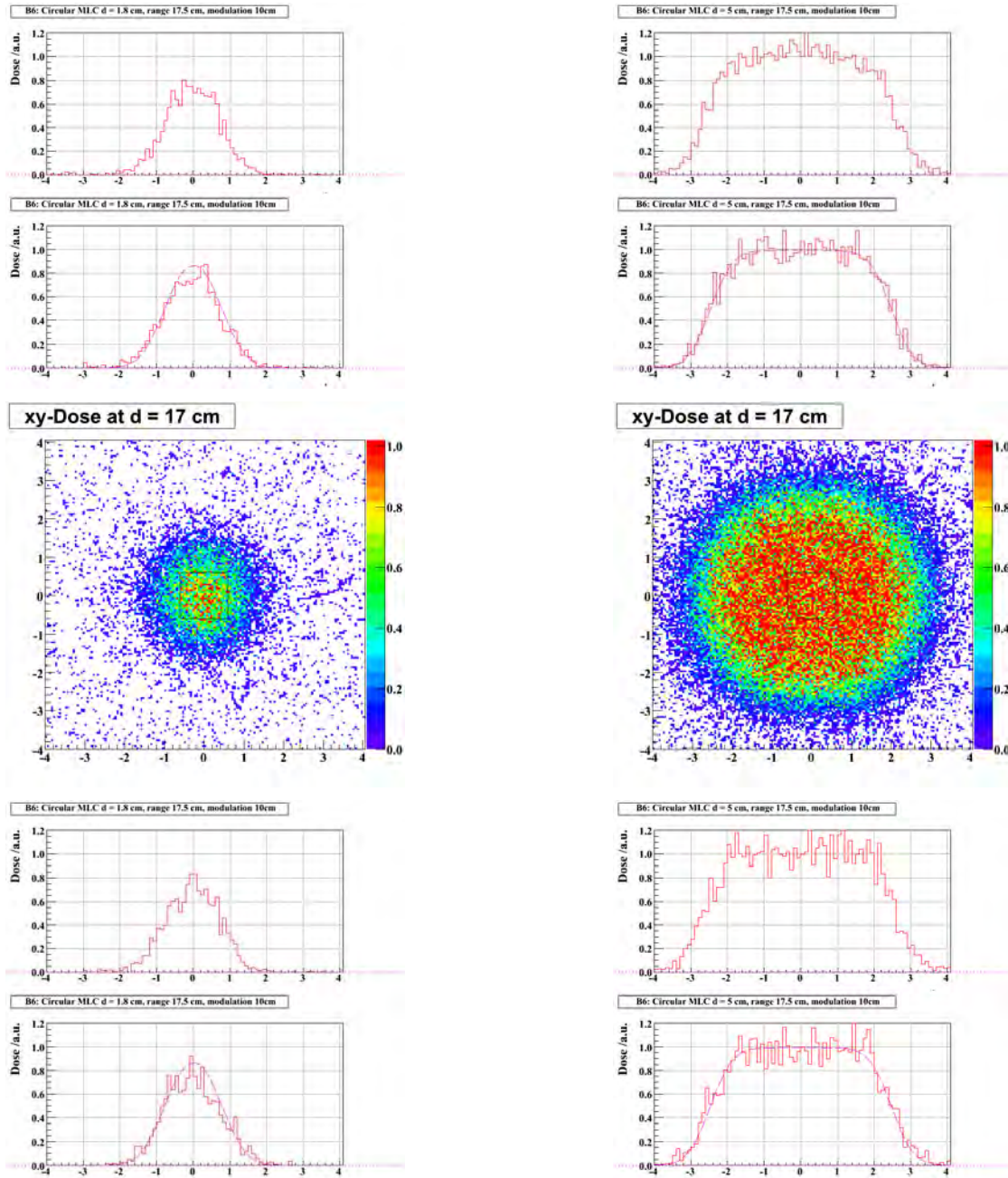
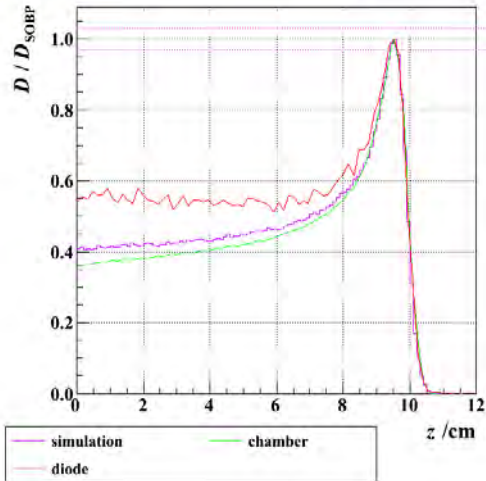
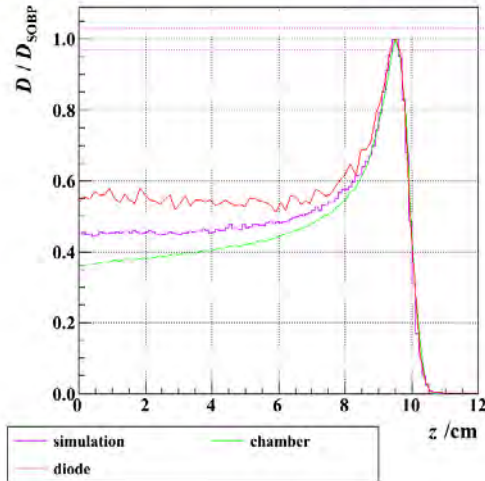


Figure A1.3: XY-dose distributions and profiles in the x- and y- direction for circular fields with diameters of 1.8 cm (left) and 5 cm (right) at depths of 0, 5, 10, 12.5, 15, and 17 cm. The beam is double scattering option B6 with a range of 17.5 cm and a 10 cm modulation. There is a square in the center of the XY-dose distributions indicates the area of integration used to create the simulated SOBPs in Figure 1. The y-profiles have the Eclipse-calculated profile at isocenter (depth = 12.5 cm) plotted for reference in purple.

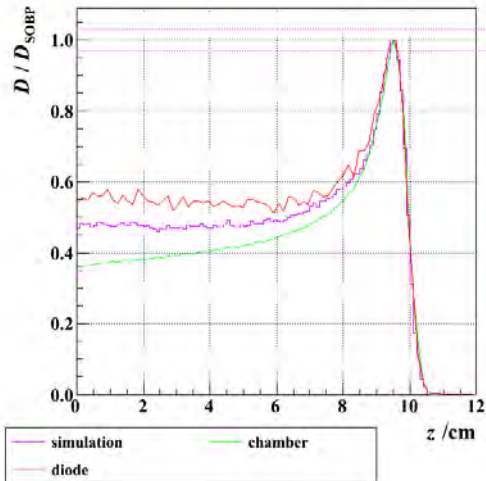
range = 9.55 cm, 12 mm integration



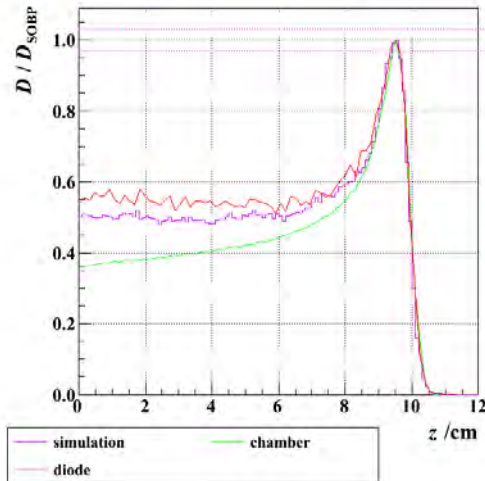
range = 9.55 cm, 10 mm integration



range = 9.55 cm, 8 mm integration



range = 9.55 cm, 6 mm integration



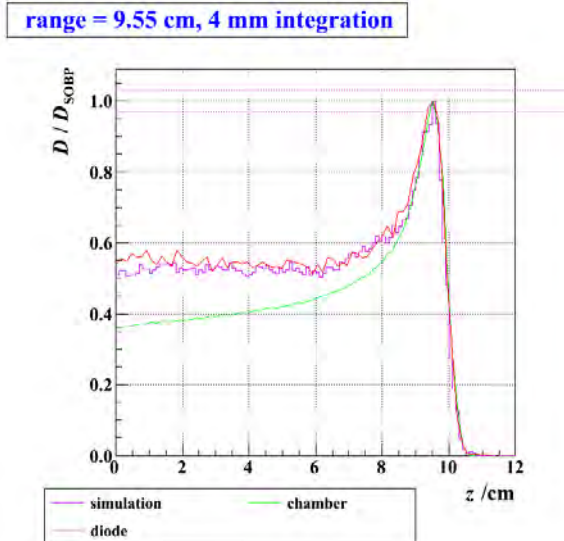


Figure AI.4: Pristine peaks using double scattering option B6 with a range of 9.55 cm and a $0.86 \times 0.86 \text{ cm}^2$ square field size comparing simulation curves (purple) with measurements taken with both a PPC05 ion chamber (green) and an SFD stereotactic diode (red). The simulated pristine peaks have been plotted using different areas of integration through the center of the water phantom. The areas that have been used are 12×12 , 10×10 , 8×8 , 6×6 , and $4 \times 4 \text{ mm}^2$. With an integration area $\sim 12 \times 12 \text{ mm}^2$ the simulation is comparable to the chamber measurement, but as the integration area decreases, the simulation gets closer to the diode measurement.

II. Simulating the compensator

At the time of our last report, we were having trouble creating patient-specific compensators in the simulation because of the complicated array of volume boundaries created when using a large number of subtraction volumes. Geant has trouble handling the tracking of particles through overlapping Boolean volumes, and because compensators have thousands of drill positions, our simulations using subtraction volumes to create the compensator were unable to finish after several days. In order to solve this problem, we decided to try to approximate the compensator such that we did not use overlapping or subtraction volumes. We did this by using the remaining thickness of the compensator at each dwell position to create a rectangular prism that did not overlap with neighboring dwell positions. A diagram of the pattern used is shown in Figure II.1. Because clinical compensators are constructed with several thousand drill positions, this approximation should not cause much difference in dose distribution.

We tested the orientation of the compensator by creating a test compensator with four different thicknesses in each corner. The test compensator was 2mm thick in the upper left corner, 20mm in the upper right corner, 40mm in the lower right corner, and 60mm in the lower left corner. The orientation of the compensator with respect to the MLC was verified by visualizing and measuring the thicknesses of the compensator using HepRep. Figure II.2 shows the XY-dose distributions at different depths for the test compensator, again verifying the orientation of the compensator created in simulation. The file used to

create this compensator had over 17,500 drill positions, meaning there were over 17,500 volumes created in the process of making the simulated compensator. In this case, where we are no longer using overlapping subtraction volumes to make the compensator, the simulation did not take much longer to run than if the same simulation had been run with the compensator absent. The simulation can now read the drill positions and remaining Plexiglas thicknesses of the compensator from a DICOM file, and create the field-specific compensators in our model.

When running patient simulations, we found that if the air-gap between the compensator and the patient was small, as for brain patients, when the CT images were reconstructed in simulation the field of view extended such that the compensator was being overwritten by air material due to the large area of air in the CT set surrounding the patient. For this reason a crop function was developed so that the CT set can be cropped around the patient and the compensator will no longer be overwritten.

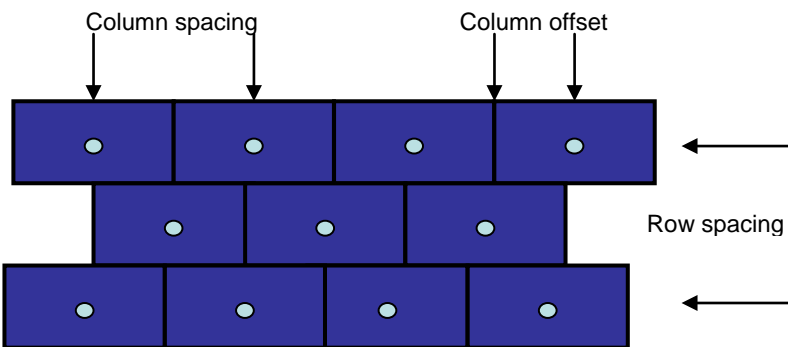
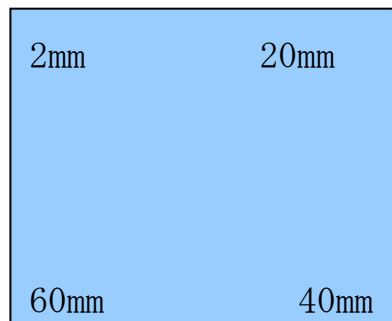
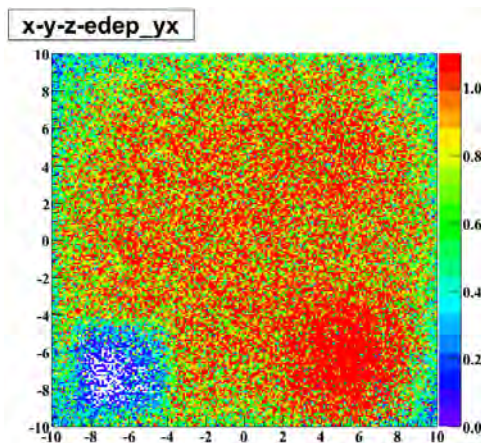


Figure AII.1: To create the compensator, the simulation reads in the row and column spacing and row offset of the drill positions from a DICOM file and creates a rectangular prism with the remaining thickness of Plexiglas at each position. Previously we had been creating the compensator by making cylindrical subtraction volumes with the milling tool diameter, but Geant was having problems handling the large number of overlapping Boolean volumes.

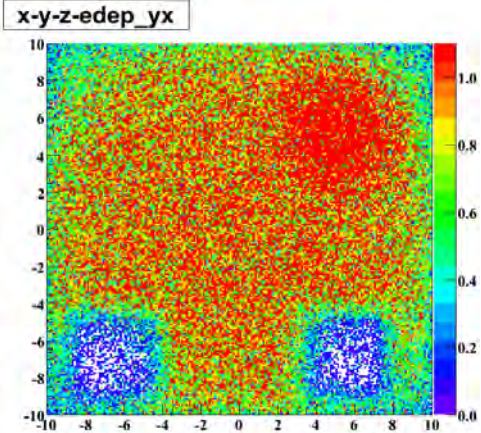
Test Pattern



Depth = 20 cm



Depth = 22 cm



Depth = 24cm

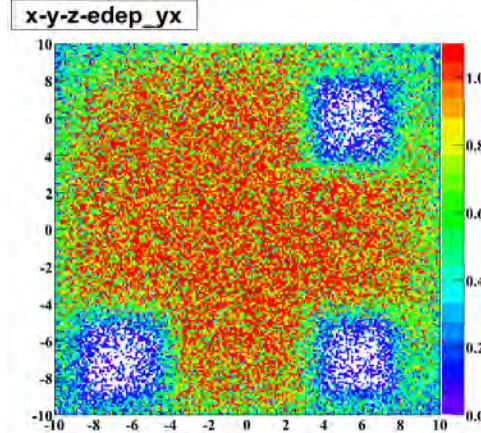


Figure AII.2: To test that the compensator is being created in the correct orientation, a test compensator was created following the pattern shown in the upper left with different thicknesses of Plexiglas at each corner using 17,555 drill positions. A beam with a range of 25 cm was sent through the compensator and the XY-dose distribution at depths of 20, 22, and 24 cm are shown here. At a depth of 20 cm in the corner where the compensator is 60mm there is almost no dose, and in the corner where the compensator is 40mm thick, the peak dose is being deposited. At a depth of 22cm, the corner corresponding to where the compensator is 40mm thick has greatly reduced dose, and in the corner where is compensator is 20mm thick, the peak dose is being deposited. This shows that the compensator is being created in simulation with the correct orientation.

III. Optimization of the Simulation Model

The last few quarterly reports have been focused on the verification of our simulation model with measured beam data so that simulations can be used in the future for clinical investigations with confidence in the accuracy of the results. At this point we have double-scattering beam data from three different treatment rooms as well as uniform scanning data from one room that we are utilizing to investigate differences between simulation results and measured data as well as to tune the simulation beam parameters such that the results produced more closely resemble measured data.

In our previous report, we discussed changing from Geant version 4.9.1 to version 4.9.3. Due to continued discrepancies between the range of the simulated beam and measured data, we have updated to the newest version of Geant (4.9.4). We had found that simulated results from version 4.9.3 closely matched the range of uniform scanning pristine peaks that were measured without anything in the beam line, indicating that it accurately modeled the beam range in water. However, once the double-scattering beam line components were added in the simulated beam line, the resulting simulated beam range was consistently deeper than the measured range. In changing the Geant version from 4.9.3 to 4.9.4 we wanted to first, verify that range of the simulated beam in water without any beam line components did not change, then check if the range of double-scattered pristine peaks were any closer to measured ranges.

As described in our previous quarterly report, pristine peaks measured during uniform scanning commissioning were compared with simulation results employing nominal spectral data provided by the manufacturer and the same beamline settings. The measured uniform scanning peaks with nothing in the beam line were used to tune the energy spectrum of the beam in the Monte Carlo such that residual differences between simulation and measurement were minimized. Because the entrance dose in simulation was found initially to be consistently lower than in measurement, a distribution of low energy protons as suggested by Bortfeld (MedPhys 1997) was added to the beam to represent protons that may have scattered from the edges of the beam pipe, but would not otherwise be accounted for in the simulation model.

Bortfeld's theory was that the beam can be split into a narrow Gaussian distribution about the mean kinetic energy of the beam and a tail of low energy protons due to scatter along the beam pipe which is a small percentage of the protons in the Gaussian. Because the fluence in the low energy tail is only a small fraction of the total beam fluence and it is expected that the fluence of protons with zero energy will be zero and there will be a positive ramp of fluence up to the mean kinetic energy, the low energy tail can be approximated using a linear ramp such that $\Phi(E) \propto E$ for $0 \leq E \leq E_0$. To better fit the widths of the pristine peaks, the sigma of the Gaussian of the beam's mean kinetic energy was also adjusted. We found that by finding the best fitting kinetic energy spread and then varying the fraction the low energy proton tail to be added, we could get the simulated pristine peaks to fit perfectly with the measured data.

The spread of the Gaussian about the mean kinetic energy had previously been set as a function of percent momentum spread which was calculated as follows:

$$\text{Percent momentum spread} = 0.00801 - 3.08E-5 * \text{Mean kinetic energy}$$

where the two parameters for this linear fit come from beam data originally provided by IBA. Several simulations were run corresponding to each of the uniform scanning measurements with nothing in the beam line varying the kinetic energy spread to find the optimal fit. The dose distribution of the low energy tail was then added to the results of the beam with the optimal kinetic energy spread to optimize the fit of simulation results to measurement.

To verify that the range in water did not change, we repeated simulations that corresponded to 9 pristine peaks taken during uniform scanning commissioning with nothing in the beamline. The results from simulations with version 4.9.4 were plotted along with measured pristine peaks and the results from simulations using Geant version 4.9.3. The results are plotted in Figure III.1 and they show that there was no significant change in the range of protons in water between the two versions.

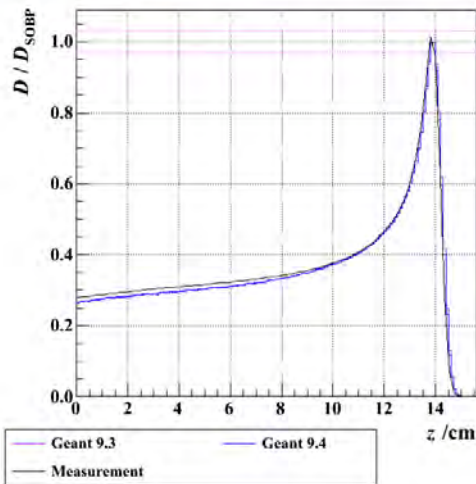
Next we wanted to check how the double-scattering SOBPs using Geant 4.9.4 looked with respect to the measurements from the three rooms that have been commissioned, so

simulations were run for a low, medium, and high energy range SOBP. Since the beam current modulation files that we are using were optimized to create flat SOBPs when we were using Geant 4.9.1, we did not expect the simulated SOBPs using Geant 4.9.4 to be flat. The results are plotted in Figure III.2 and the same results using Geant 4.9.3 are plotted for comparison to show that the newer version made an improvement concerning the range of double-scattering SOBPs.

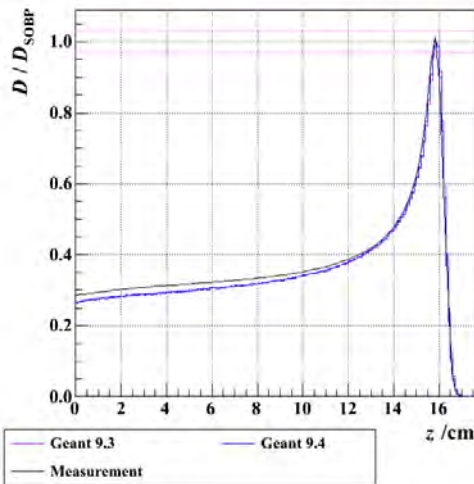
All of the double-scattering pristine peaks that were measured during commissioning of rooms 1, 3, and 5 were also simulated using Geant 4.9.4. The simulations were run incorporating the optimized kinetic energy sigma and fraction of the low energy proton distribution that were described in the previous report. These simulations were run to check the range of the simulated results and to see how the fit for the kinetic energy sigma and low energy proton distribution, which were optimized to fit uniform scanning pristine peaks, affected the double-scattering simulations results. The simulations results are plotted in Figure III.3 with the measured pristine peaks for each of the three treatment rooms for comparison. Table III.1 lists the nominal distal 90% range, the average range from commissioning measurements in three treatment rooms, and the ranges from simulation. It also lists the difference between the range from the simulation results (versions 4.9.1 and 4.9.4) and measured range, and the differences are plotted as a function of nominal range in Figure III.4.

For each of the Geant versions that we have tested for use in our simulation (4.9.1, 4.9.3, and 4.9.4) the water-equivalent thickness (WET) of the second scatterers and modulator wheel have been found by running simulations for each of the double-scattering options first with nothing in the beam line, and then with each of the components being placed in the beam line. The WET of the components is of interest because, as mentioned previously, the simulated range is equal to the measured range in water when there is nothing in the beam line, but when looking at double-scattering measurements, the simulated range is too long. This means that the range of the beam is not being reduced by the same amount in simulation as in reality while traveling through the beam line components. Table III.2 contains the WET of the second scatterers and modulator wheels given by IBA and the WETs found in simulation for each double-scattering energy options for each of the Geant versions that we have tested.

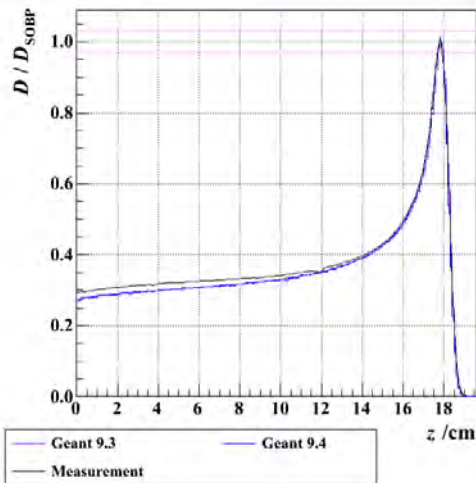
US2 range = 14 cm



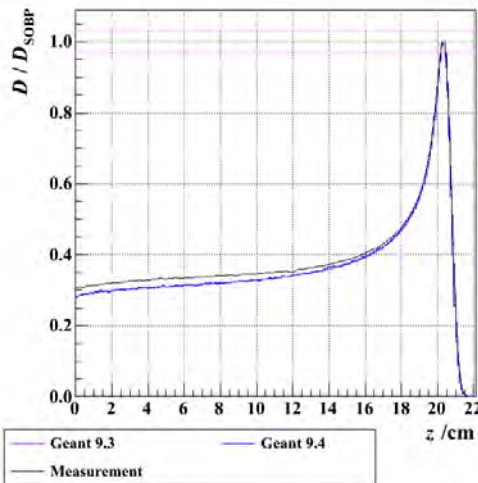
US2 range = 16 cm

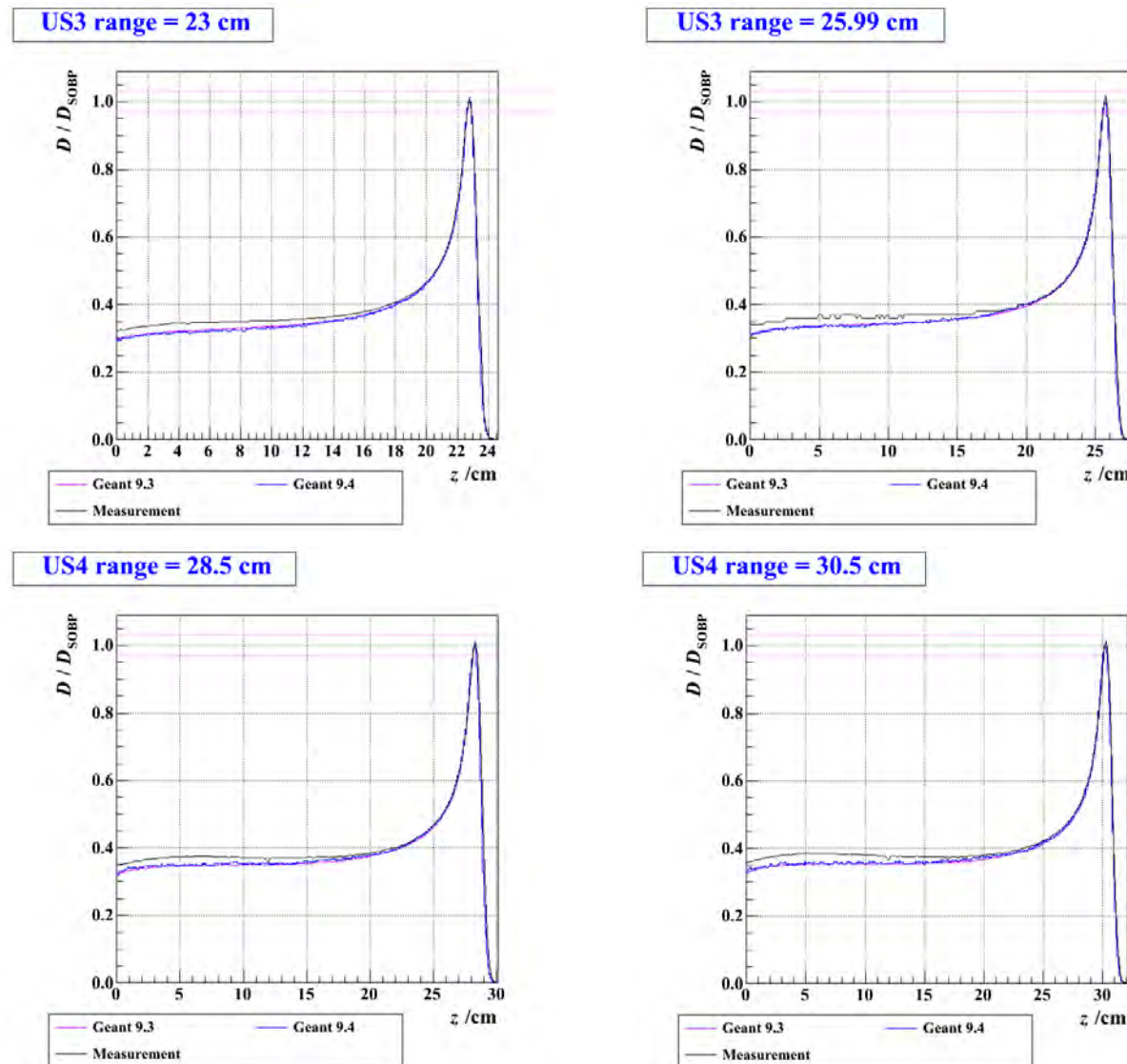


US2 range = 18 cm



US3 range = 20.5 cm





US4 range = 32.14 cm

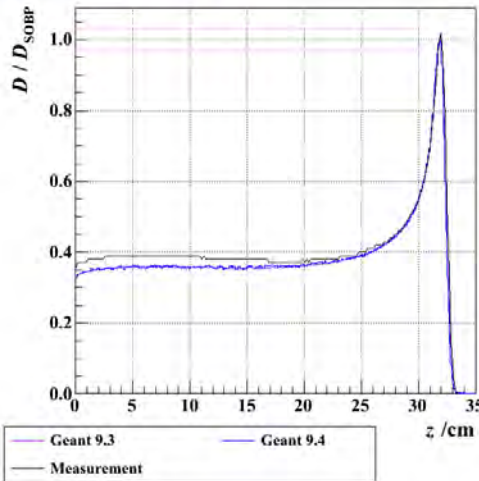
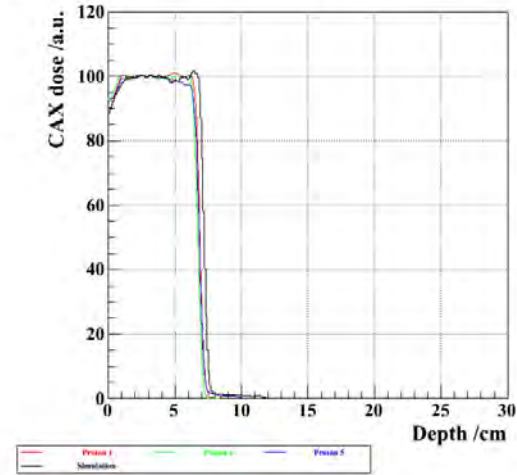


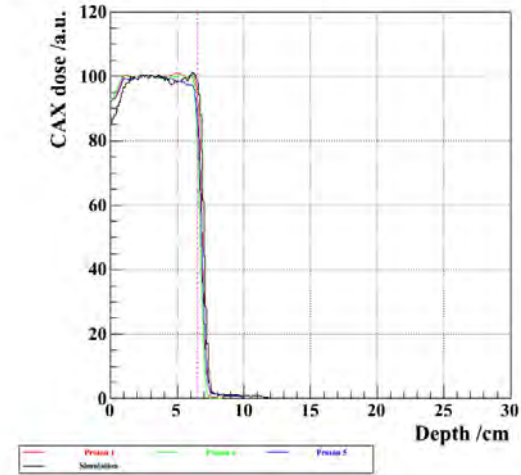
Figure AIII.1: Uniform scanning pristine peaks simulated with Geant 4.9.3 (purple), Geant 4.9.4 (blue) plotted with measured pristine peaks (black) to verify that the range in water between the two versions does not change. Measurements and simulation were done with a $10 \times 10 \text{ cm}^2$ square field size with a $40 \times 40 \times 40 \text{ cm}^3$ water tank. For these particular ranges in uniform scanning there are no scatterers in the beam line and the beam does not travel through the modulator wheel. The simulations were run using the newly optimized kinetic energy spread mentioned in the previous report.

II.

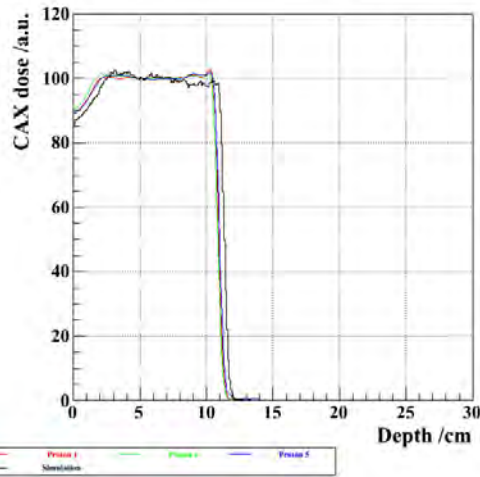
B2: range = 6.5 cm, modulation = 6.5 cm



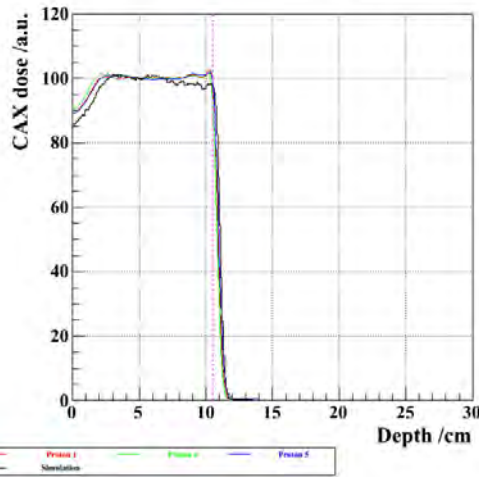
B2: range = 6.5 cm, modulation = 6.5 cm



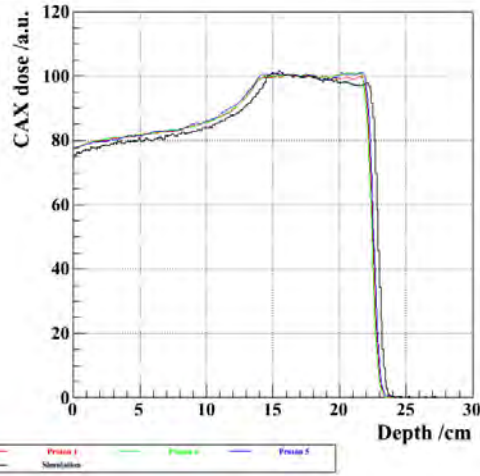
B4: range = 10.5 cm, modulation = 10.5 cm



B4: range = 10.5 cm, modulation = 10.5 cm



B7: range = 22 cm, modulation = 10 cm



B7: range = 22 cm, modulation = 10 cm

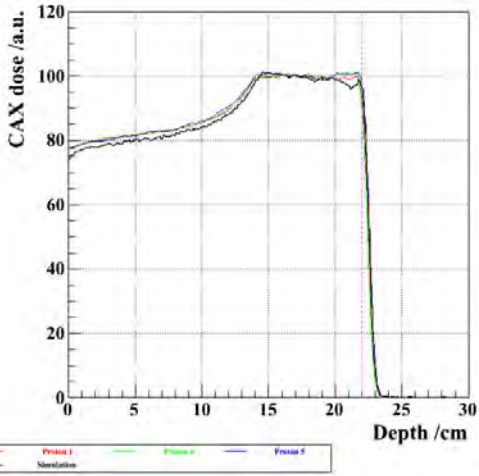
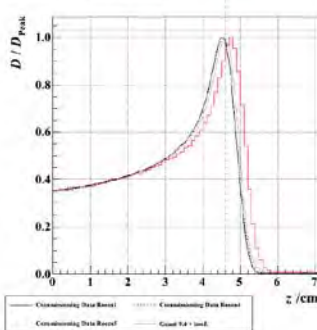


Figure AIII.2: Double-scattering depth dose curves for SOBPs that have been measured during commissioning for rooms 1, 3, and 5 plotted with results from simulations using Geant 4.9.3 (left) and Geant 4.9.4 (right). The simulation results are plotted in black.

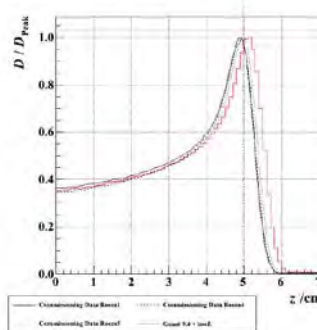
III.

IV.

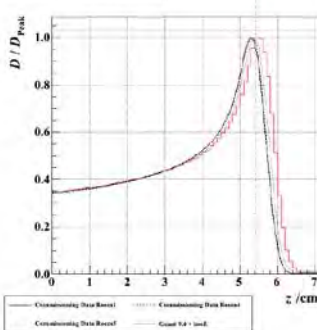
B1 range = 4.60 cm

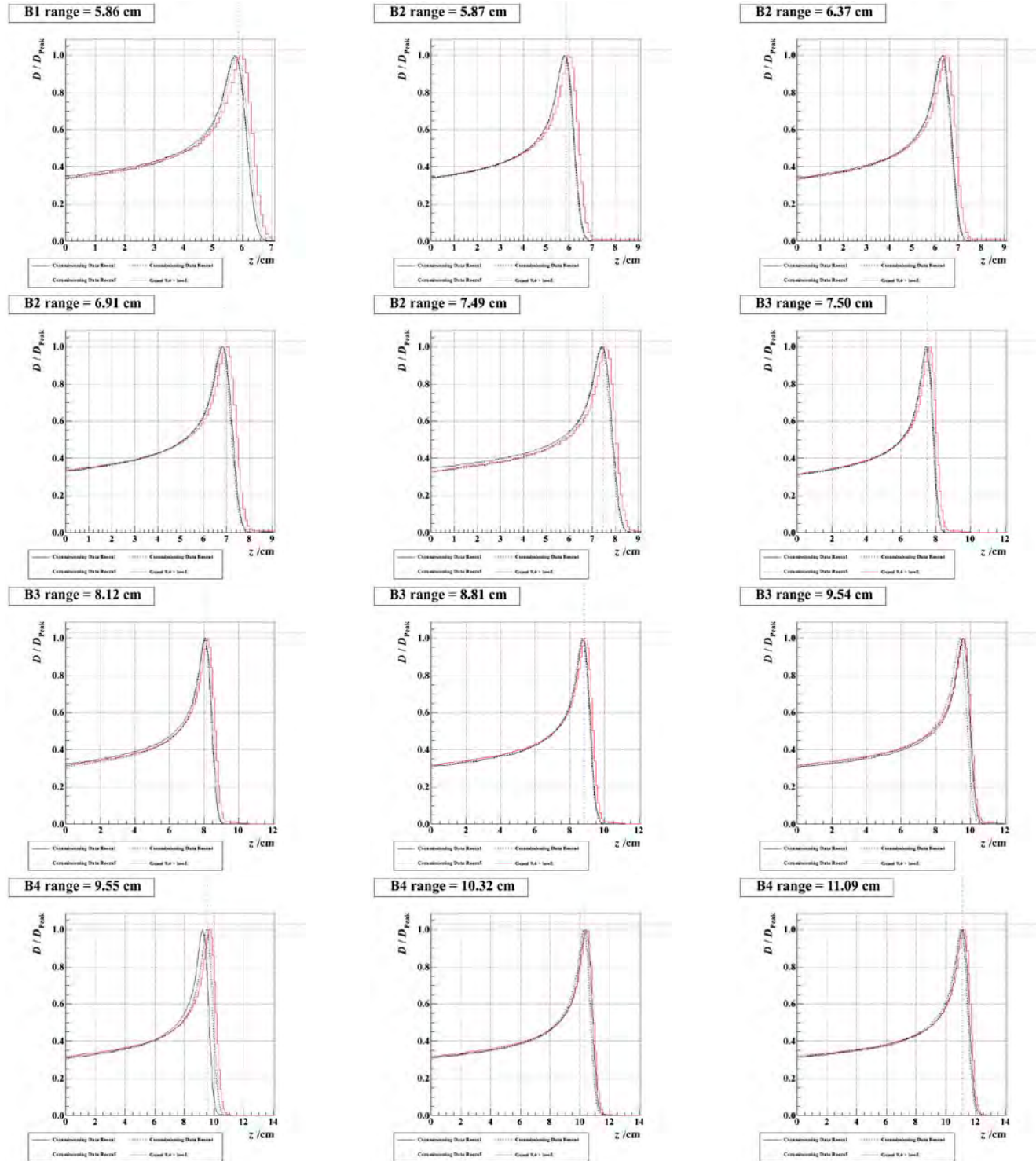


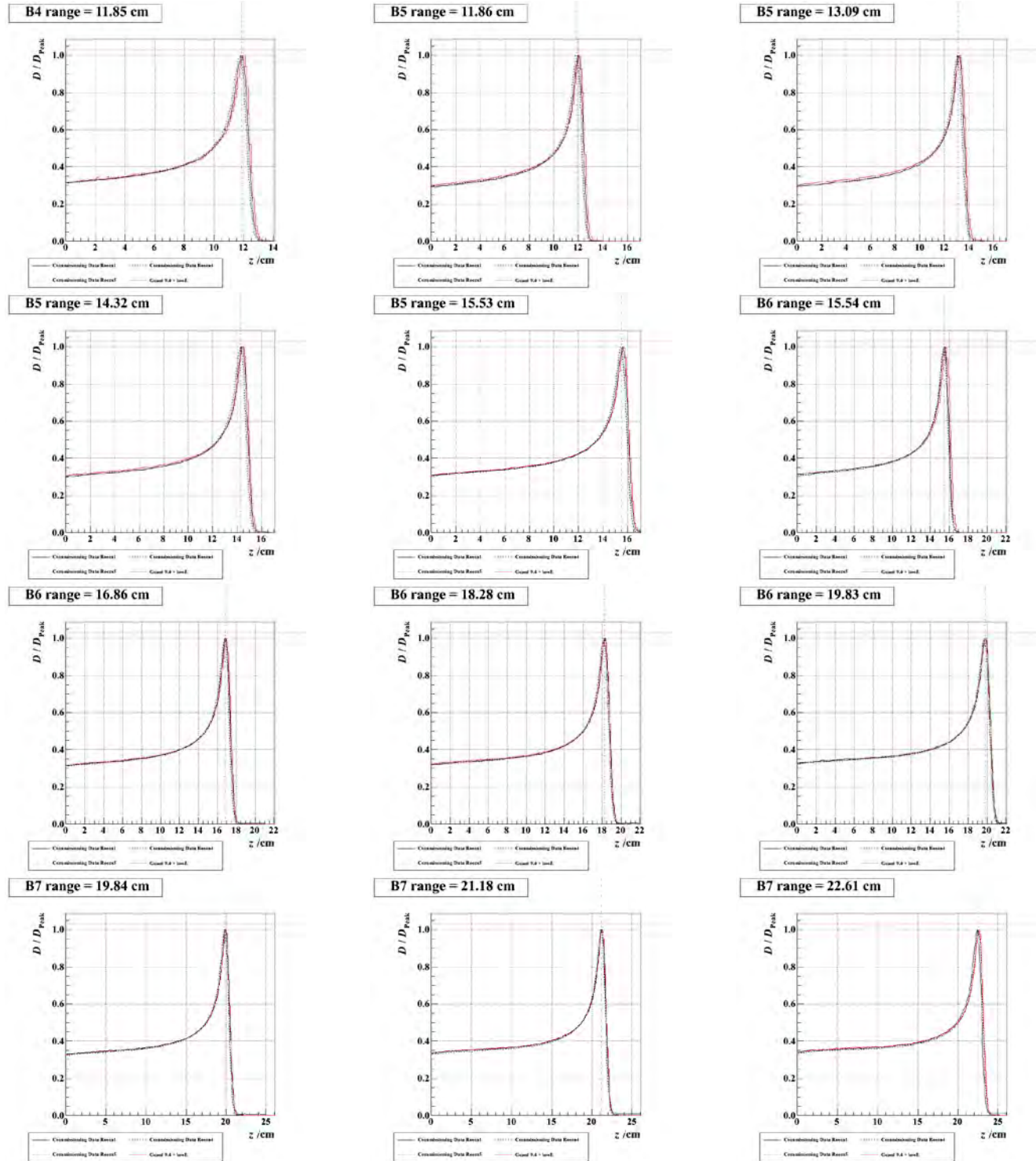
B1 range = 4.99 cm



B1 range = 5.41 cm







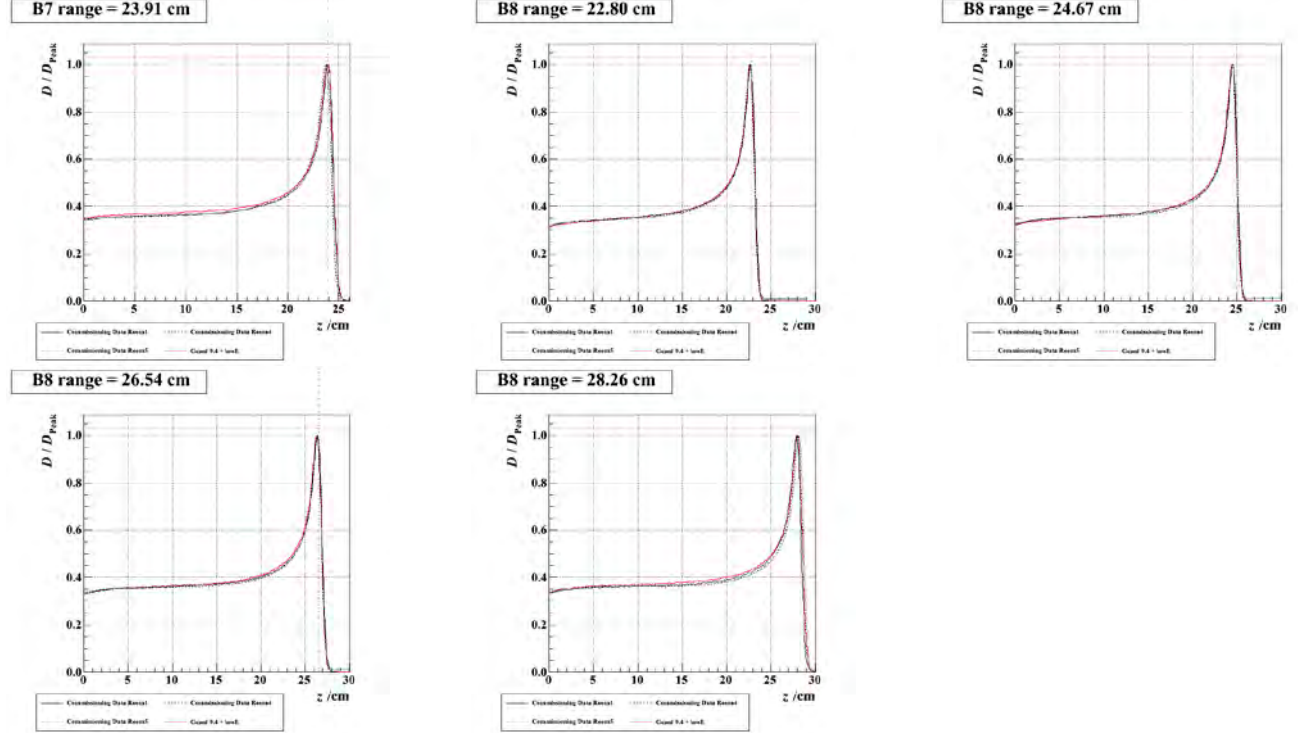


Figure AIII.3: Double-scattering pristine peaks that have been simulated using Geant 4.9.4 with the newly optimized sigma of the kinetic energy Gaussian about the mean kinetic energy and the added distribution of low energy protons. Simulation results are plotted in red while the commissioning measurements from the three treatment rooms are plotted in black.

Table AIII.1: Summary of ranges from double-scattering pristine peaks

	Nominal Range	Avg Measured(P1,4,5)	G9.1	G9.4	G9.1-MeasuredAvg	G9.4-MeasuredAvg
B1	4.6	4.647	5.1	4.9	0.453	0.253
	4.99	5.040	5.5	5.3	0.460	0.260
	5.41	5.450	5.9	5.7	0.450	0.250
	5.86	5.910	6.3	6.2	0.390	0.290
B2	5.87	5.933	6.3	6.2	0.367	0.267
	6.37	6.423	6.9	6.7	0.477	0.277
	6.91	6.957	7.4	7.2	0.443	0.243
	7.49	7.553	8	7.8	0.447	0.247
B3	7.5	7.587	7.9	7.8	0.313	0.213
	8.12	8.183	8.5	8.4	0.317	0.217
	8.81	8.887	9.2	9.1	0.313	0.213
	9.54	9.620	9.9	9.8	0.280	0.180
B4	9.55	9.540	10	9.9	0.460	0.360
	10.32	10.443	10.8	10.7	0.357	0.257
	11.09	11.217	11.6	11.4	0.383	0.183
	11.85	11.950	12.3	12.2	0.350	0.250
B5	11.86	12.030	12.2	12.3	0.170	0.270

	13.09	13.243	13.4	13.5	0.157	0.257
	14.32	14.477	14.6	14.7	0.123	0.223
	15.53	15.677	15.9	15.9	0.223	0.223
B6	15.54	15.640	15.8	15.9	0.160	0.260
	16.86	16.977	17.1	17.2	0.123	0.223
	18.28	18.383	18.5	18.6	0.117	0.217
	19.83	19.960	20.1	20.1	0.140	0.140
	20.1	20.17	20.1	20.2	0.083	0.183
B7	21.18	21.350	21.5	21.5	0.150	0.150
	22.61	22.690	23.1	22.9	0.410	0.210
	23.91	24.020	24.1	24.2	0.080	0.180
	22.8	22.873	22.9	22.9	0.027	0.027
B8	24.67	24.730	24.7	24.7	-0.030	-0.030
	26.54	26.590	26.6	26.6	0.010	0.010
	28.26	28.237	28.3	28.3	0.063	0.063

V.

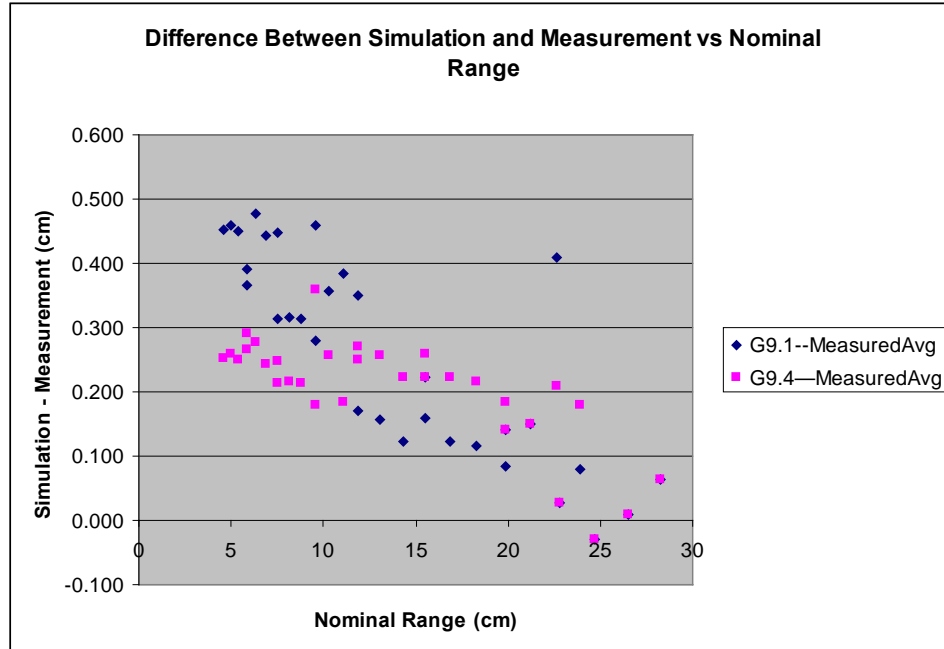


Table AIII.2: List of simulated and IBA-provided WET of the second scatterers and modulator wheels for each of the double-scattering options using each Geant version we have tested.

Geant 4.9.1

	MC WET SS	IBA WET SS	Difference(cm)	MC WET ModWheel	IBA WET ModWheel	Difference (cm)
B1	6.1	6.2000	-0.1	4.7	4.83	-0.13
B2	6.2	6.2500	-0.05	4.7	4.83	-0.13

B3	6.1	6.2500	-0.15	1.7	1.78	-0.08
B4	6.2	6.2800	-0.08	2.2	2.23	-0.03
B5	3.5	3.6000	-0.1	1.7	1.78	-0.08
B6	3.5	3.6100	-0.11	2.2	2.23	-0.03
B7	3.6	3.6400	-0.04	2.9	2.83	0.07
B8	0.8	0.8400	-0.04	1.9	1.89	0.01

Geant 4.9.3

	MC WET SS	IBA WET SS	Difference(cm)	MC WET ModWheel	IBA WET ModWheel	Difference(cm)
B1	6.1000	6.2000	-0.1	4.6	4.83	-0.23
B2	6.1000	6.2500	-0.15	4.6	4.83	-0.23
B3	6.1000	6.2500	-0.15	1.6	1.78	-0.18
B4	6.1000	6.2800	-0.18	2	2.23	-0.23
B5	3.3000	3.6000	-0.3	1.6	1.78	-0.18
B6	3.3000	3.6100	-0.31	2	2.23	-0.23
B7	3.4000	3.6400	-0.24	2.7	2.83	-0.13
B8	0.8000	0.8400	-0.04	1.7	1.89	-0.19

Geant 4.9.4

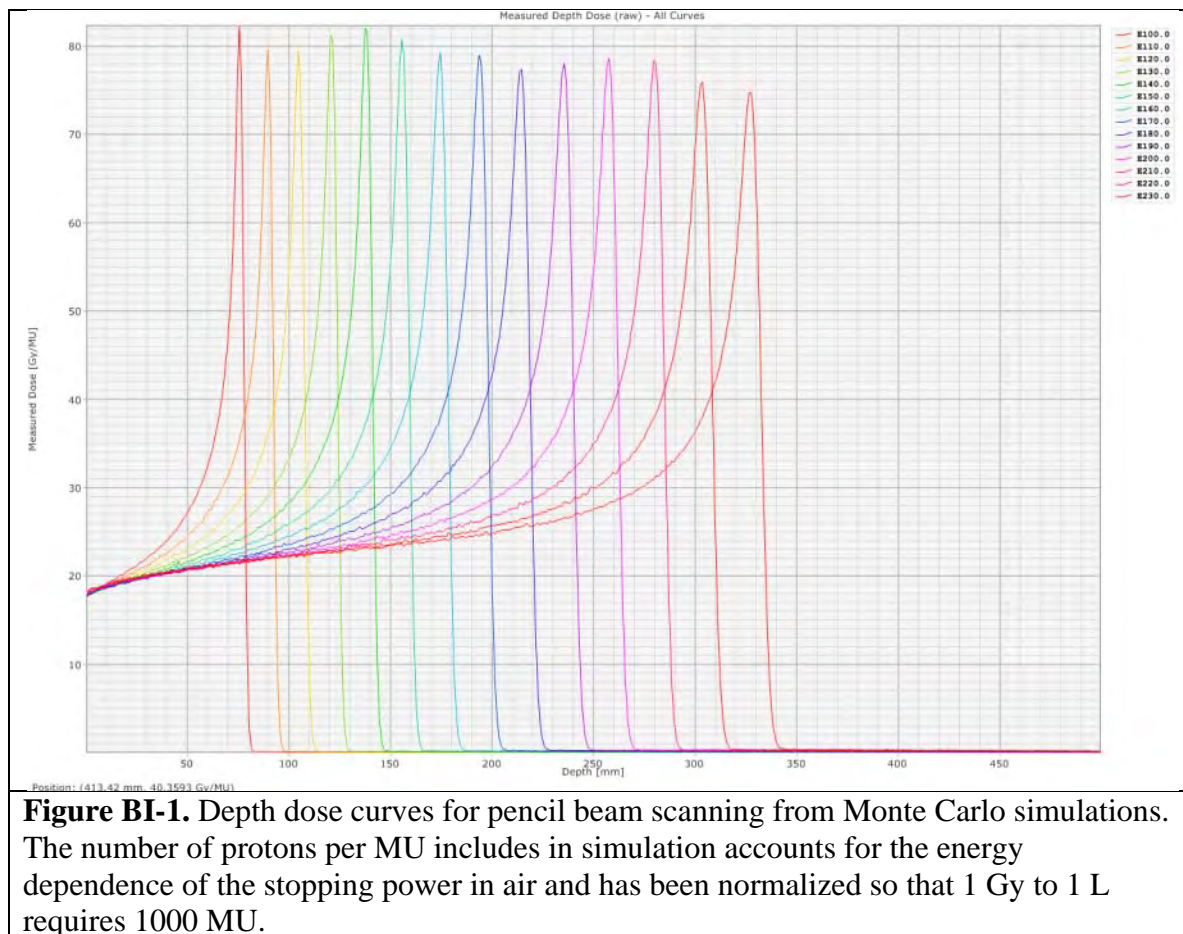
	MC WET SS	IBA WET SS	Difference(cm)	MC WET ModWheel	IBA WET ModWheel	Difference(cm)
B1	6.2000	6.2000	0	4.7	4.83	-0.13
B2	6.2000	6.2500	-0.05	4.7	4.83	-0.13
B3	6.2000	6.2500	-0.05	1.6	1.78	-0.18
B4	6.2000	6.2800	-0.08	2.1	2.23	-0.13
B5	3.5000	3.6000	-0.1	1.7	1.78	-0.08
B6	3.6000	3.6100	-0.01	2.1	2.23	-0.13
B7	3.5000	3.6400	-0.14	2.7	2.83	-0.13

B 8	0.8000	0.8400	-0.04	1.7	1.89	-0.19
--------	--------	--------	-------	-----	------	-------

B. Spot Scanning Progress

I. Eclipse Plan Verification with Monte Carlo

A major accomplishment of the Phase II research this past year is the development of software that, given a patient CT dataset and a treatment plan file from the Eclipse treatment planning system, performs the calculation of the 3D dose distribution in patient using the Geant4 Monte Carlo engine. This is called the *forward* dose calculation: given the beam delivery specification (from the treatment plan file), the dose to the patient is determined. (The inverse calc is to determine the delivery parameters from the desired dose distribution in patient.) For the case of pencil-beam scanning, the Eclipse treatment planning system was commissioned with Monte Carlo generated beam profiles and depth dose curves. The 7.5 cm acrylic range shifter used to treat shallow depths was also simulated and commissioned in Eclipse. In order to calibrate the number of simulated protons per MU, a reference condition was calculated with Eclipse: a 10 cm x 10 cm x 10 cm target within a water phantom was brought to 1 Gy and the number of protons per MU was adjusted to make the total number of MU for this reference condition treatment plan equal to 1000. This is different than the reference condition previously quoted, 100 MU for 1 Gy/L, that is in use at MD Anderson. The particular value is not important, as long as it is known and stable, and that the absolute dose calibration factor (Gy/MU) is measured accurately. The value of 1000 was recommended by IBA, and the specs quoted by IBA like the minimum number of MU per spot and the resolution of the monitor chambers assume this definition for MU. The depth range for the reference condition is 11 cm to 21 cm depth. For simulations, the number of protons per MU should be a function of MU, because the monitor chamber response is determined by the stopping power of protons in air, which is a function of energy, but also the mean path length of particles through the monitor chamber will be a function of energy: the lower energy beams have a larger beam emittance and will tend to have a slightly large path length. The second effect has not yet been included in simulation. The first effect has been included by incorporating the stopping power in air into the calculation of the number of protons per MU. A function of the form $A + B/E * \ln E$ is motivated by taking the non-relativistic limit of the intermediate-energy term of the Bethe-Bloch equation. The parameters A and B were obtained by PSLR fit to data from NIST PStar. It is interesting that the stopping power in air decreases by about a factor of 2 over the range of 100 MeV to 230, and that the height of peak of the proton depth dose curve is reduced by nearly the same factor of 2 due to range straggling in such a way that the two effects balance (at least over this energy range), and a plot of Bragg peaks of different energies have roughly the same Gy/MU in the peak (see Figure I-1).



We can perform the forward dose calculation using our in-house PBS simulation code based on the Geant4 Monte Carlo engine. We will use these simulations to validate the dose calc algorithms in Eclipse and to tune parameters in Eclipse that have an effect on fits of the commissioning data and parameters affecting the optimization engine. Derek has commissioned Eclipse with simulated data using the universal and dedicated nozzle codes so that planning studies can proceed with Eclipse. Projects are underway at Penn to investigate the quality of PBS plans, in terms of how to optimize PBS plans; how plan quality can be improved with fine beam control, range shifters and/or bolus, possibly lateral spreaders; and how PBS plans will compare to other modalities for specific disease sites (currently, prostate, head and neck, breast, rectal, and pancreatic cancers). An example of the PBS forward calculation using Geant is shown in Figure I-2. The dose-volume-histograms (DVH) for the Monte Carlo plan is much worse than the Eclipse-calculated plan. This is due to at least two reasons. The Monte Carlo calc needs to be run with more primaries for higher accuracy. Dose is accurate to only 2-5% in the PTV (see Figure I-3). The random statistical noise in the Monte Carlo dose distribution blurs the DVH line for target coverage. Still, the median dose to the PTV is shifted in Monte Carlo. This is believed to be the effect of the dose halo. Eclipse is modeling the proton beam with a single Gaussian, but there is a Rutherford tail to the profile due to

nuclear interactions (E Pedroni et al 2005 *Phys. Med. Biol.* 50 541 doi: 10.1088/0031-9155/50/3/011). Figure I-4 shows the distribution of the difference-of-dose between Monte Carlo and Eclipse. The two calculations mostly agree in the center of the PTV. Around the margin of the PTV, Monte Carlo is about 5% lower than Eclipse, and a little further outside the PTV Monte Carlo is 5% higher. This is consistent with the idea that some of the Gaussian peak has been scattered out to a longer tail that Eclipse is not modeling. Within Eclipse, it is possible to include a second Gaussian term in the model of the beam profile, but there is a parameter that must be tuned to adjust the relative weight of the two Gaussians. This was discussed at PTCOG with Armin Langenegger, one of Varian's physicists, who did not think this parameter was necessary for IBA pencil beam. This second Gaussian was added for the Hitachi beamline at MD Anderson. Next year, Derek will continue a study comparing the pencil beam profile at depth between Eclipse and Monte Carlo calculations.

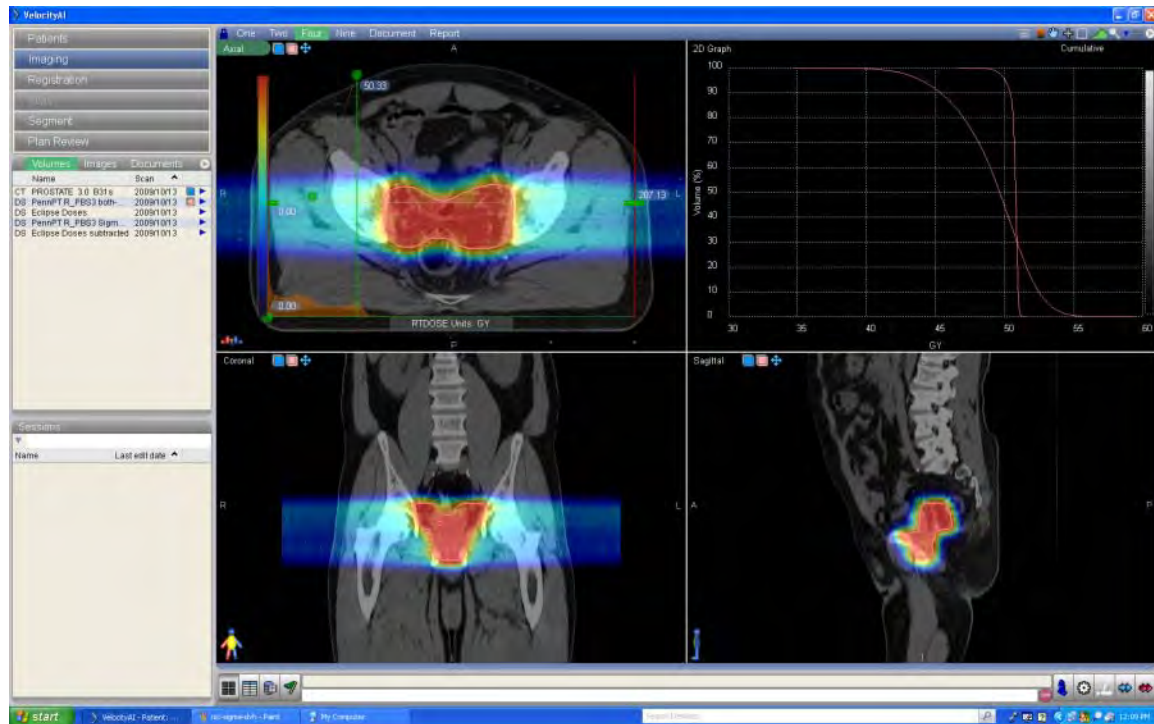


Figure BI-2. Dose distribution for a prostate case calculated with Geant4 Monte Carlo simulations. Note that the DVH line for target coverage is much worse for the Monte Carlo calc than for the Eclipse dose calc. This is due mostly to the sample variance contribution to the Monte Carlo dose uncertainty, which can be reduced by running longer simulations. The median dose for the Monte Carlo calc is only 49 Gy rather than the 51 Gy that Eclipse gives.

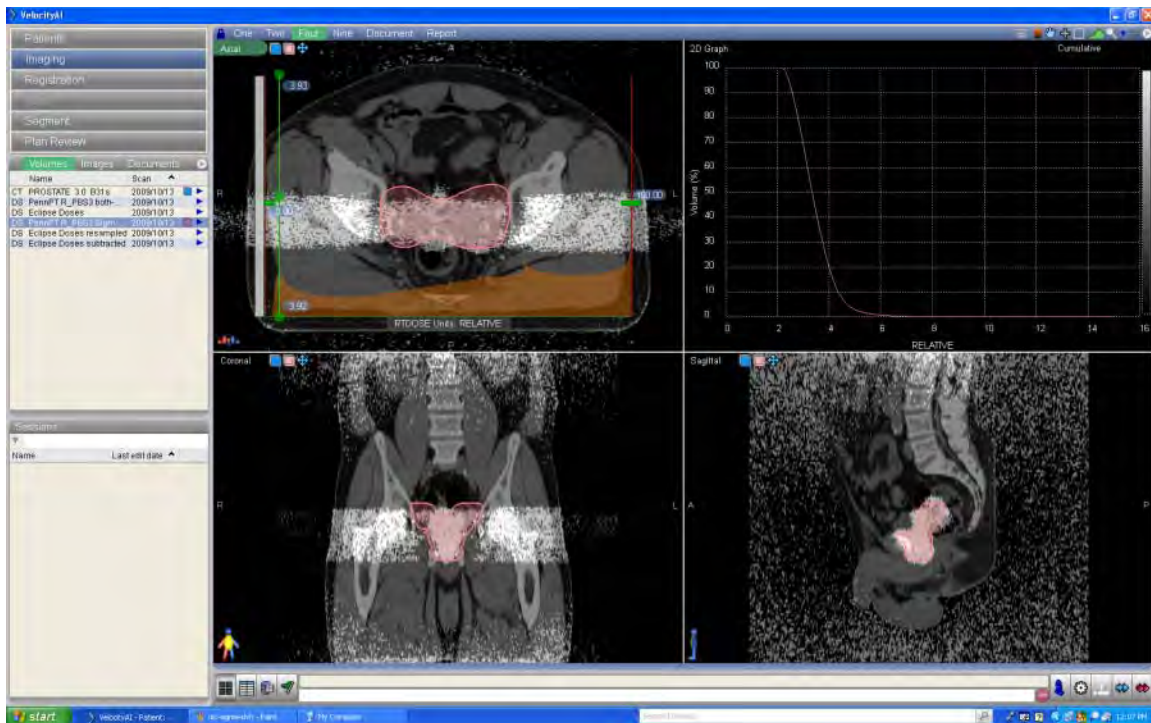


Figure BI-3. Dose uncertainty distribution for the prostate case in Figure I-2. This distribution essentially represents the error bars for the dose shown in Figure I-2. Note that the uncertainty shown here currently only includes the contribution of random sample variance inherent from the Monte Carlo method. No contribution is included for setup uncertainties, motion, target delineation, or other uncertainties. The white areas have uncertainty less than 4%. The top right panel is the analogue of DVH: an uncertainty volume histogram. It shows that the target dose is accurate to between 2 and 5%. The relative sample variance scales as $1/\sqrt{\text{dose}}$, so the most uncertain points will be at the margin of the PTV, as can be seen top left where some of the PTV is not white, i.e. $> 4\%$ sigma.

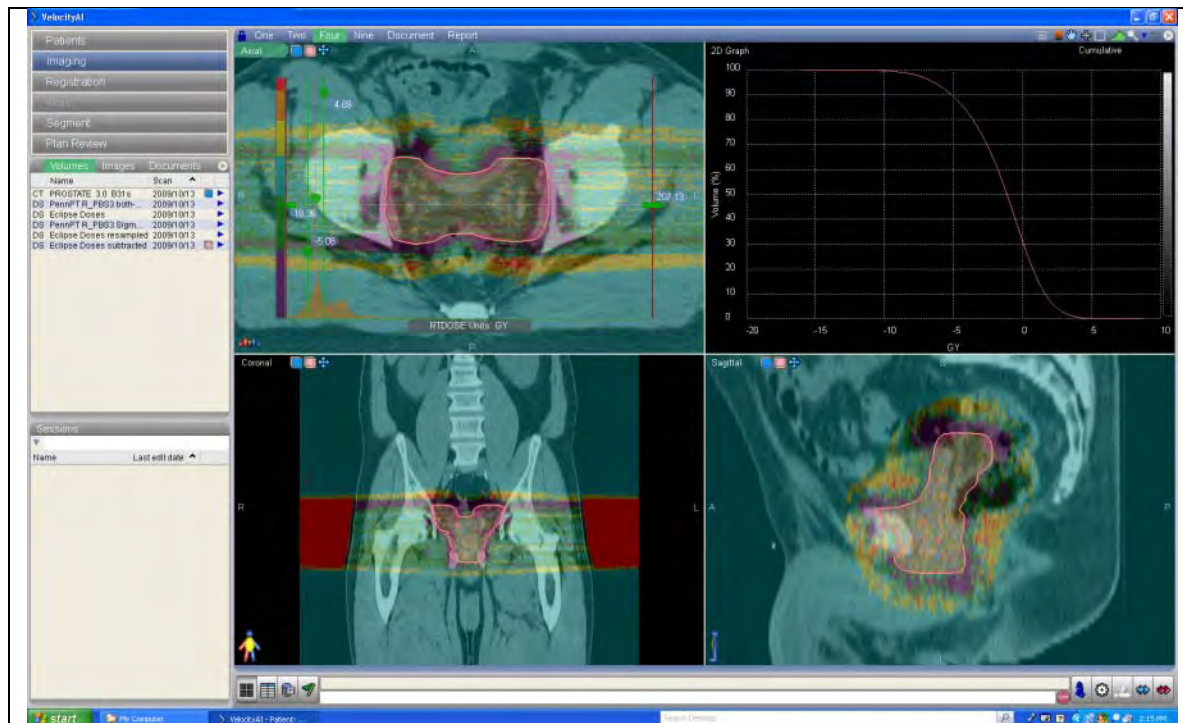


Figure BI-4. Distribution of the dose difference between Monte Carlo and Eclipse. A positive difference indicates that the dose from Monte Carlo simulation is larger than the dose from Eclipse. Red areas are where Monte Carlo is 5 Gy (10 % of prescription) higher than Eclipse, purple areas are where Monte Carlo is 5 Gy lower than Eclipse. Simulation is showing that near the margin of the PTV, the dose is generally about 10% lower than Eclipse (the purple border), and then about a centimeter beyond the margin it is 10% higher (the red/orange halo). We believe this is the effect of a dose halo that Monte Carlo is getting right, but Eclipse is failing to reproduce.

We can also do the forward calc for double-scattering and uniform scanning plans. Chris Ainsley has been developing the simulation code for the universal nozzle since he began in 2006. He has been primarily concerned with double-scattering mode, and so his simulation code includes the scatterers, the modulator wheels, and more recently the MLC and patient-specific compensator. Derek has incorporated the voxelized phantom based on patient CT data into the Chris's universal nozzle code. These new options were added to the macro file for universal-nozzle simulations:

```
# -----
# detectorType:
# 0 = none
# 1 = readout (default)
# 2 = voxelized patient (need to specify CTDataPath)
# 3 = gas chamber layer
# -----
```

/beamLine/Phantom/detectorType	2
/beamLine/Phantom/CTDataPath	ct/datafiles/
/beamLine/Phantom/planFile	
ct/datafiles/PBS2/RN.1.2.246.352.71.5.1794135381.322230.20100326105405.dcm	
/beamLine/Phantom/structureFile	
ct/datafiles/PBS2/RS.1.2.246.352.71.4.1794135381.25548.20100326105458.dcm	
/beamLine/Phantom/bodyContour	BODY

These commands setup a voxelized geometry based on the dicom CT datafiles in the path ct/datafiles/. The geometry is properly oriented in the beamline based on the isocenter, gantry angle, and other data in the dicom plan file. The plan file also contains the MLC shape and compensator pattern. The bodyContour is just used to set the material to air outside the specified structure. The voxelized CT geometry code has been discussed in previous reports and will not be repeated here.

Maura Kirk implemented the C++ class to write out dicom RT Dose files. This means that dose scored on the voxelized patient CT geometry can be written to a dicom file that can be opened by a dicom viewer, registered with the CT data, with dose drawn as colorwash, manipulated in 3D, allowing point measurements, DVHs to be calculated, and support taking differences between dose maps which will be useful as we start to compare Eclipse calculated dose with simulations. We are using Velocity AI to open the dicom files (CT data and Monte-Carlo-calculated RT Dose files). Velocity can also open dicom structure files, and plot the physician-drawn contours with the CT and dose data. An example is shown in Figure I-1 where a Monte Carlo dose calculation is being compared to the Eclipse calculation in Velocity. The plan in the Figure was calculated with Eclipse, exported as a DICOM file used as input to our Monte Carlo code, which outputs a DICOM RT Dose file that can be read and displayed with Velocity.

We continue to refine our implementation of the IBA nozzles in simulation to reach better agreement with data collected during commissioning of the proton treatment rooms. So far we have double-scattering and uniform scattering data from 4 of our treatment rooms. We will begin accepting the last room, which is dedicated PBS, in the summer of 2011. We are relying on IBA's specifications for spot-size and beam emittance to generate realistic beam data using Monte Carlo that can be used to commission Eclipse for research purposes. For the simulation of pencil beam delivery, it was learned that the use of Fermi-Eyges approximations for the multiple scattering contribution is not adequate to determine an initial phase space for the simulations. We had used Fermi-Eyges theory to quickly compute for each beam energy a phase space for a proton beam focused to a specified spot size at isocenter (see Quarterly Report for the 1/1/09-3/31/09 period). Fermi-Eyges assumes that the beam profile is double-Gaussian and remains so even after propagating through material. The multiple-scattering implementation in Geant4 uses a different theory, Lewis theory, that is exact in the sense that any errors in the moments of the multiple-scattering distributions can be traced back to approximations made to the differential cross section. Lewis theory computes the lateral moments as well as the angular, whereas Fermi-Eyges only provides the angular

moments. Lewis theory does not assume that the beam profile is Gaussian, nor does a Gaussian profile necessarily remain Gaussian after multiple scattering. We found that if we use Fermi-Eyges to estimate the multiple-scattering to determine an initial phase space, using that phase space for Geant4 simulations does not result in a beam of the proper spot size and position of the double waist. Derek Dolney wrote some simulation code to track an infinitesimal, monoenergetic pencil beam through air and fit a function to the multiple-scattering contribution as a function of depth in air. This fit is now used instead of Fermi-Eyges to get the multiple-scattering right for Geant4 simulations in order to produce a beam of the right transverse dimensions, within 0.4% (see Figures I-5 and I-6).

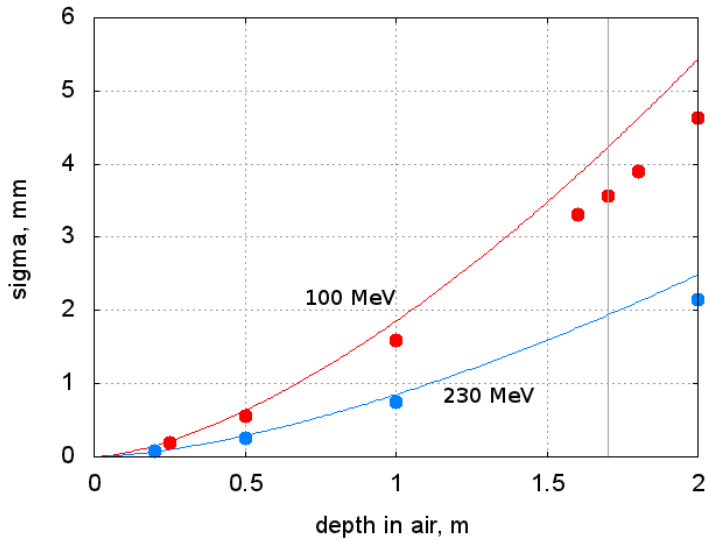


Figure BI-5. Contribution to the beam sigma due to multiple scattering as a function of depth in air. The lines represent the Fermi-Eyges calculation, the spots are Geant4 simulations which use Lewis scattering theory. Fermi-Eyges overestimates the scattering in air, so that if a phase space is constructed using the Fermi-Eyges estimate, the double waist of the simulated beam will be deeper than was desired, as can be seen in Figure I-6.

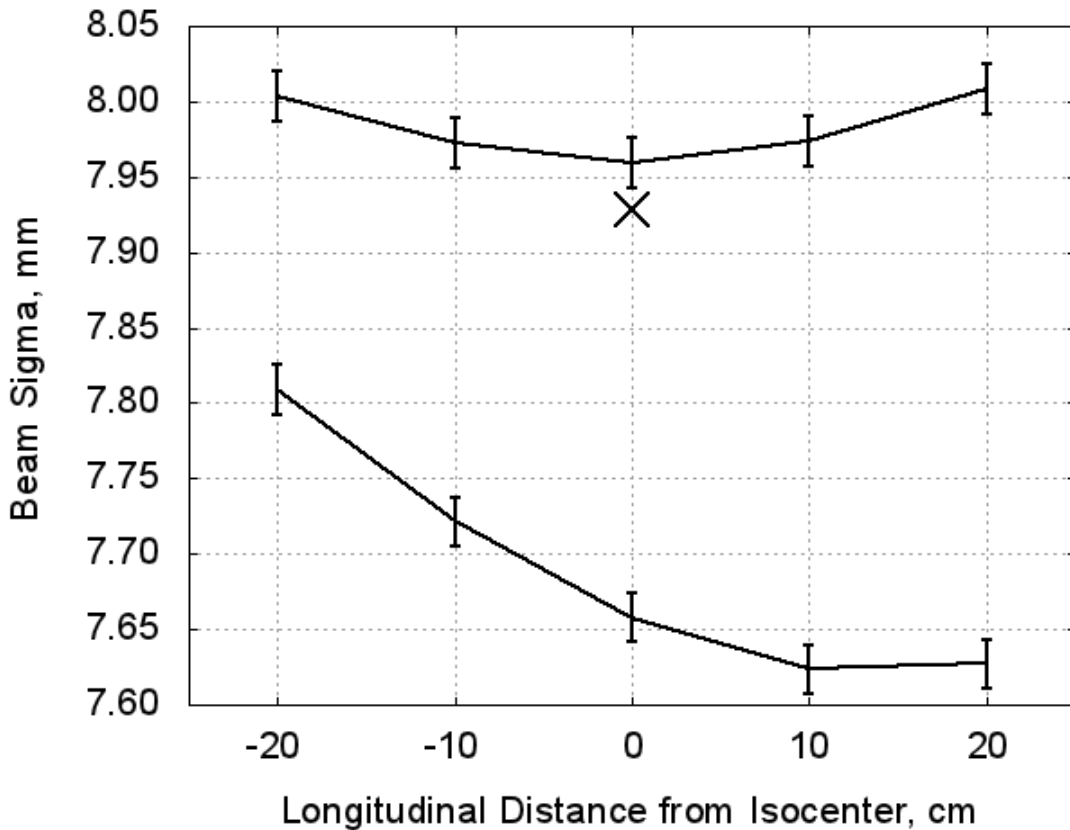


Figure BI-6. Spot size near isocenter from simulations using a primary phase space calculated with Fermi-Eyges (lower line) vs. using a fit to the multiple-scattering-in-air contribution from Geant4 simulations. The target spot size at isocenter is indicated by the X. Fermi-Eyges overestimates the multiple scattering in air, so that when a phase space is calculated with Fermi-Eyges, the simulated waist lies at a greater depth in air.

Derek has implemented the geometry for the IBA dedicated nozzle in Geant4 and determined a phase space for primaries. This nozzle results in a smaller spot size because the entire nozzle is evacuated (Figure I-7). Initial phase space was found, using the procedure described above, to fit the IBA specification spot size at isocenter.

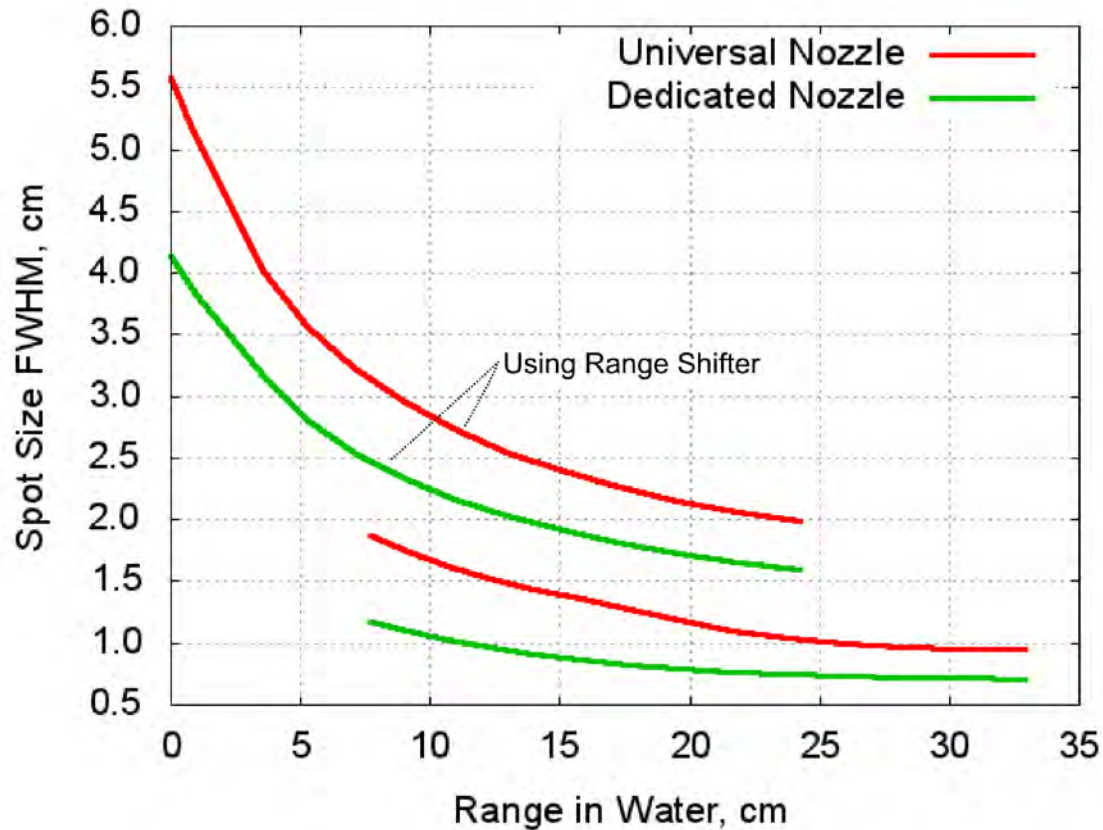


Figure BI-7. Spot size for the two IBA nozzles as a function of range in water. Also shown is the spot size when the 7.5 cm acrylic range shifter for treating shallow depths is inserted into the beam line.

Derek implemented in simulation the 7.5 cm range shifter solution that IBA is using to treat shallow targets with pencils beams. Derek generated commissioning data and learned how to commission Eclipse with range shifter data and to setup and calculate treatment plans that use the range shifter. Our treatment planning system is commissioned with Monte Carlo data for the universal nozzle and dedicated nozzle, including the range shifter, and we have begun to perform studies that compare PBS treatment plans with double-scattering plans and with IMRT plans. Several abstracts were submitted to PTCOG and ASTRO for pancreatic, head and neck, breast, and rectal plan comparison studies.

Next year will be a very exciting time, as we will finally have PBS data to validate the Monte Carlo simulations. We expect some refinements to the nozzle will be necessary. Certainly it will be necessary to generate new initial phase space data since IBA is saying that beam is not perfectly focused at isocenter but as much as 20 cm upstream. This can be accommodated easily by the procedure described above and in previous reports once the data is available. Perhaps we will also find that some of the simplifications we have made (geometric rather than true magnetic beam steering, for example) are too simplistic

and need to be improved. Until the data comes, we still have differences between Eclipse dose calc and Monte Carlo that need to be understood.

II. Development of a Micromegas layer for proton dosimetry in 2D

Derek Dolney has worked on the design and simulation of a system of detectors for three-dimensional dosimetry in proton beams. The proposed detector system is based on a type of ionization chamber called Micromegas. Micromegas uses a micromesh screen held at high voltage to achieve signal amplification in a relatively thin gas chamber (see Figures II-2, II-3, and II-4). The ionization current can be collected on a pixelated anode for 2D dose resolution. Three-dimensional resolution is obtained by stacking multiple 2D planes back-to-back. Very large systems of Micromegas detectors are used in high-energy physics experiments for high-resolution particle tracking, but the dose rate is smaller than the dose rate in the proton Bragg . It should be possible to achieve a Micromegas design for a proton therapy beam that achieves the same high-resolution, but does not saturate in the Bragg peak, by reducing the gain. The signal gain is a function of operating potentials, gap thicknesses, and gas mixture and pressure. There is already some data in the literature about the dependence of the gain on these parameters, and it is expected, based on the energy deposit in the detector obtained from Monte Carlo simulations (see Figure II-10), that a successful design can be achieved. Eventually, multiple Micromegas layers stacked back-to-back would provide 3D dose resolution.

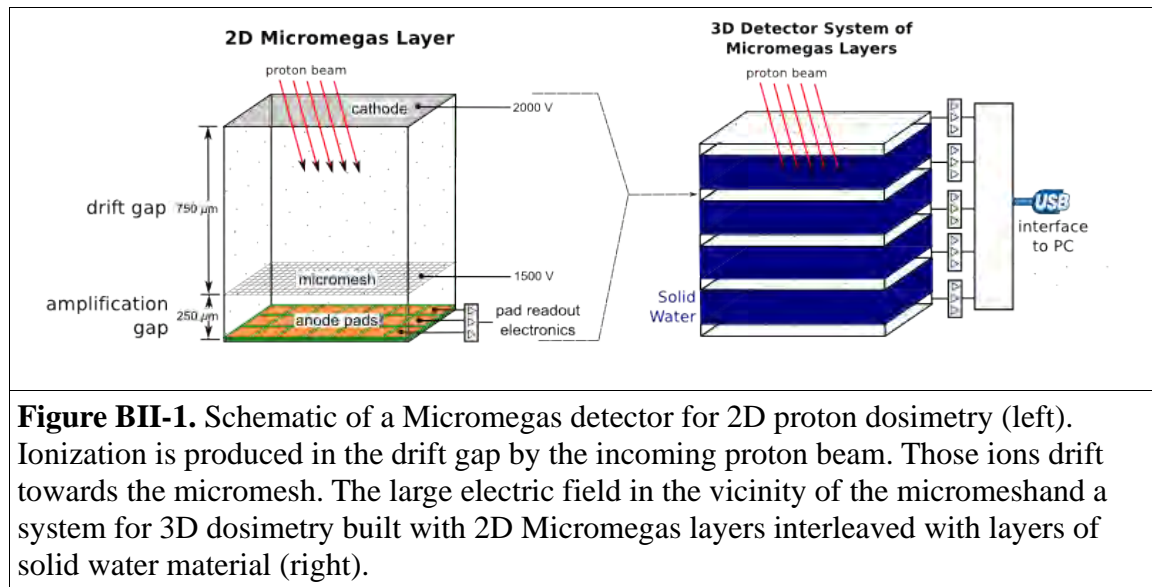


Figure BII-1. Schematic of a Micromegas detector for 2D proton dosimetry (left). Ionization is produced in the drift gap by the incoming proton beam. Those ions drift towards the micromesh. The large electric field in the vicinity of the micromesh and a system for 3D dosimetry built with 2D Micromegas layers interleaved with layers of solid water material (right).

A prototype Micromegas chamber has been assembled in the Department of Physics at the University of Pennsylvania (Figures II-2, II-3, II-4). Currently the anode is a single channel. This prototype is current in a testing phase at in the Physics Department.



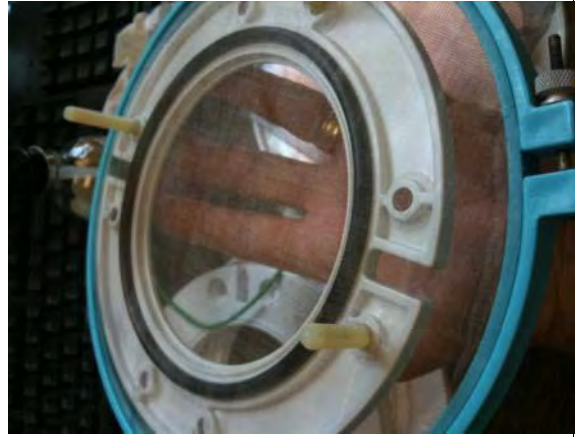
Figure BII-2. Pictures of the Micromegas detector prototype assembled in the Department of Physics at the University of Pennsylvania. **Left:** the gray rings seal the electrodes and micromesh with O-rings. Gap spacings can be changed by mounting the electrodes and/or the mesh in different slots in the gray mounting rings. A wire for one of the high-voltage electrodes is visible. **Right:** with one of the electrodes removed, the micromesh is visible inside the chamber.



Figure BII-3. Pictures of the Micromegas detector prototype assembled in the Department of Physics at the University of Pennsylvania. **Left:** the inner blue ring maintains tension on the micromesh to prevent it from deforming in the electric field. **Right:** another view of the micromesh. Also visible are the additional slots in the gray

spacing rings that allow the gap thicknesses to be varied.

Figure BII-4. An earlier, unsatisfactory attempt to prevent deformation of the micromesh in the electric field. The outer blue ring was tightened to the gray spacing rings to secure the mesh. This caused the mesh to buckle, rather than pull flat, and was abandoned in favor of the ring in Figure II-3 (left). One of the sealing O-rings (black) can be seen in this photo.



Two experiments are underway to calibrate the gas gain of the detector system: 1. An Fe-55 source is being used to calibrate the gas gain, and 2. High-energy electron beams produced by the linear accelerators in the Department of Radiation Oncology are minimum ionizing, or nearly so, and can be used to obtain a gas gain curve. We need to characterize the gas gain for Micromegas in a proton beam so that design choices such as operating potentials, gas composition and pressure, and gap thicknesses can be made. We can use simulations and theory to relate the detector response to electrons with the response to protons, though we also verify with measurements. A low-voltage gain curve is shown in Figure II-5. We used an electrometer to provide the bias voltage. The electrometer only goes up to 500 V. We need higher voltage to find the proportional region of the response curve. We have external power supplies that will go to 5 kV, and obtained a special adapter from IBA Dosimetry in order to operate our electrometer in a grounded input mode that will work with an externally supplied bias. Derek found the response curve to be essentially flat to 4500 V. Above that level the prototype began arcing and could not be used reliably. A second prototype was built (see below) that has some engineering improvements that should allow stable operation at higher voltages.

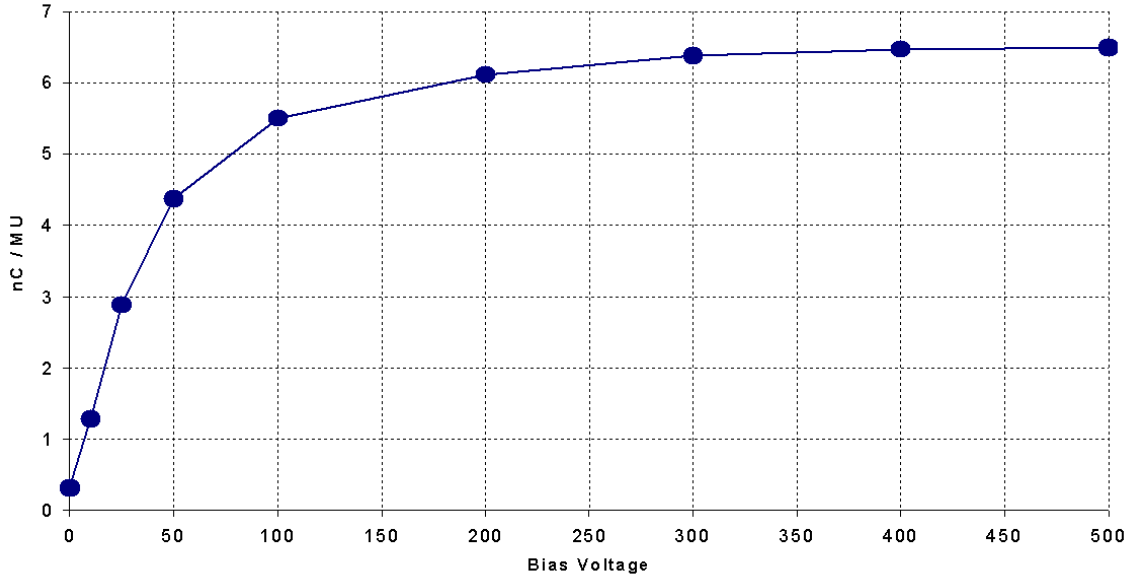


Figure BII-5. Gain curve for the prototype Micromegas chamber in a 20 MeV electron beam.

Some data has been collected with the prototype Micromegas detector in the proton beam, and in electron beams. Initially, a brief look at the reproducibility of the prototype in the proton beam was considered. Those results are given in Figure II-13. The response of the detector slowly decreases over time. We believe this is due to a space-charge effect: charge is collecting on non-conducting surfaces in the prototype assembly, such as the o-rings and plastic chamber housings, thus lowering the local electric field. The problem appears to be reduced by operating at a higher bias (300V). The next prototype will have guard ring to better shape the field around the edge of the detector so that charge is collected on the electrodes rather than accumulating on insulators.

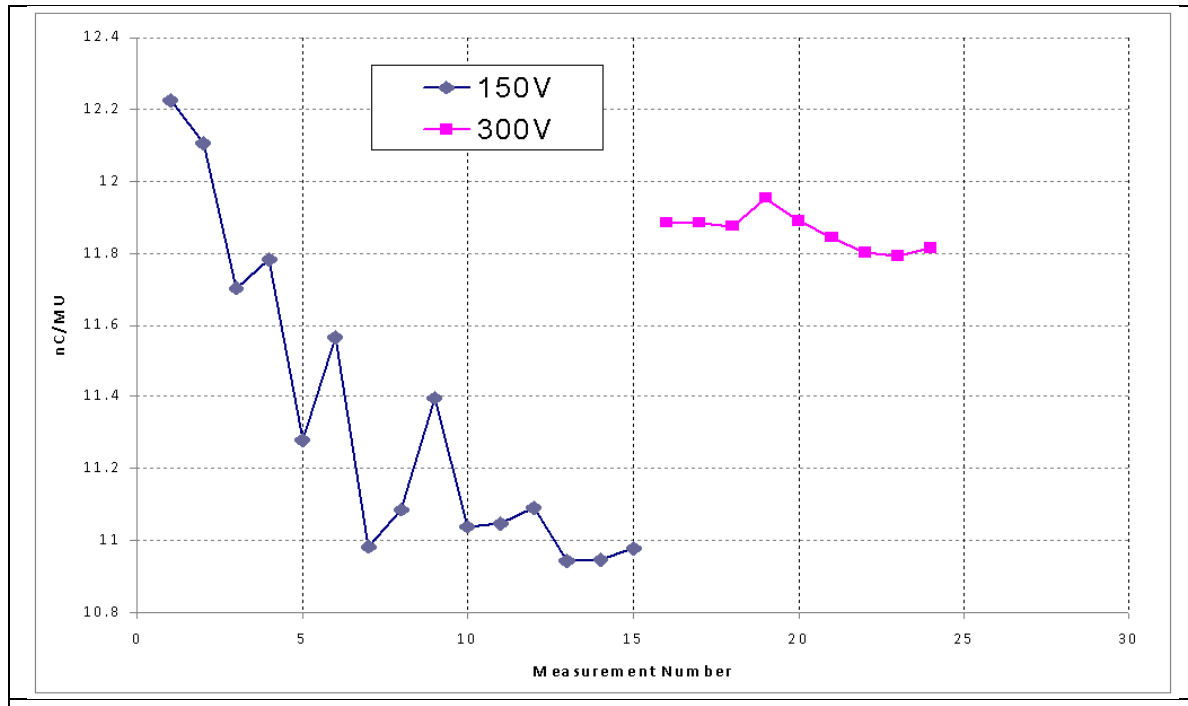


Figure BII-6. Measurements with the prototype detector at two bias voltages, attempting to establish measurement reproducibility in terms of charge collected per proton beam monitor unit (MU). At 150 V, the detector response decreases with time, suggesting that we are collecting charge on the non-conductive materials around the edges of the detector active volume, the so-called “space-charge effect”. Operating at 300 V seems to give better reproducibility. Our second prototype will have a guard ring to more efficiently collect charge near the edges.

A proton depth dose curve was measured with the prototype Micromegas detector (Figure II-7) and compared with the depth dose measured with the commercial PTW "Bragg Peak Chamber". The two curves were normalized in the entrance region (at about 8 cm) and shifted relative to each other in the depth direction, because the range is not well determined for this type of delivery. The aim was to verify that a Micromegas design does not saturate in the high dose rate within the Bragg peak. The data plotted in Figure II-7 suggests that we are on the right track, but a more careful measurement is needed. We need to take more data points in the vicinity of the Bragg peak with the prototype.

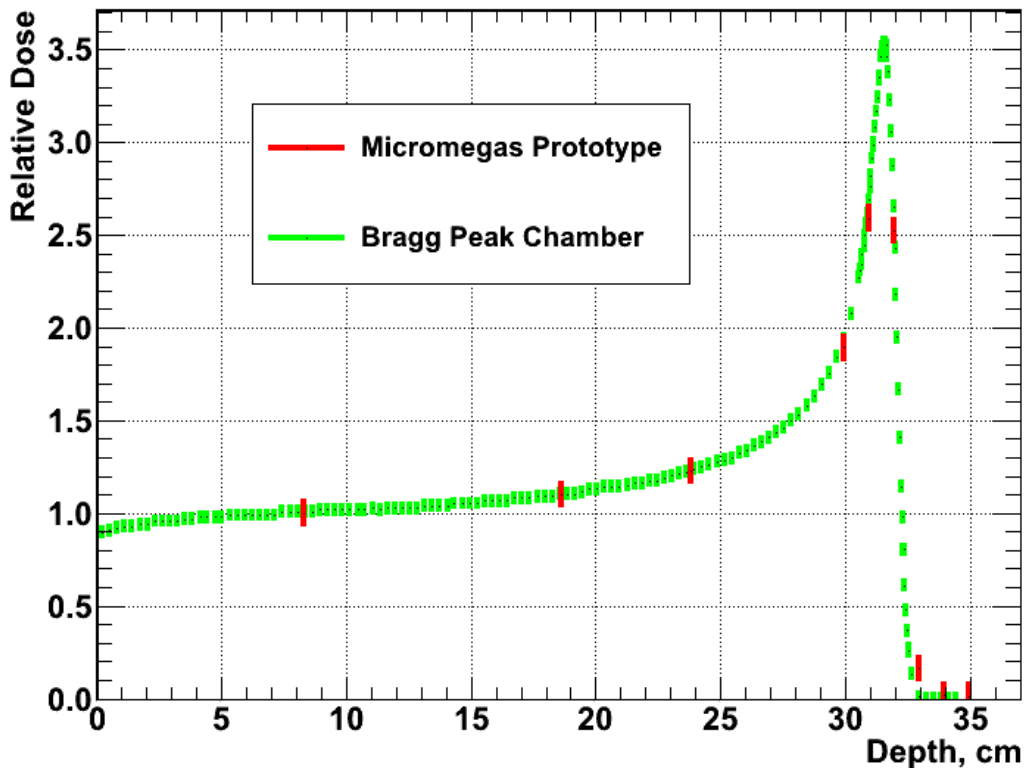


Figure BII-7. A measurement of a proton pristine Bragg peak with the prototype chamber. A measurement taken with the PTW Bragg Peak chamber is shown for comparison. The curves are normalized in the entrance region at 8 cm. The two measurements were shifted in the depth direction due to the range uncertainties associated with this type of beam delivery.

A second-generation prototype has been assembled by Professor Robert Hollebeek's group in the Physics Department. This prototype has several improvements over the first one. The most significant difference is that the cathode of the new prototype is segmented into 16 strips so that we can begin to make measurements to determine spatial resolution for this Micromegas application. This second pilot device also has several high voltage and mechanical improvements. This second device will also allow us to have one device we can put in the beam and still keep one on the test stand. Eventually we will make a prototype with pads. The electronic readout for the strips is under construction and there is an un-segmented plane that can be used in the meantime. The whole assembly can be taken apart in a few minutes and the ring arrangement allows us to quickly change the spacing of the cathodes and screen.

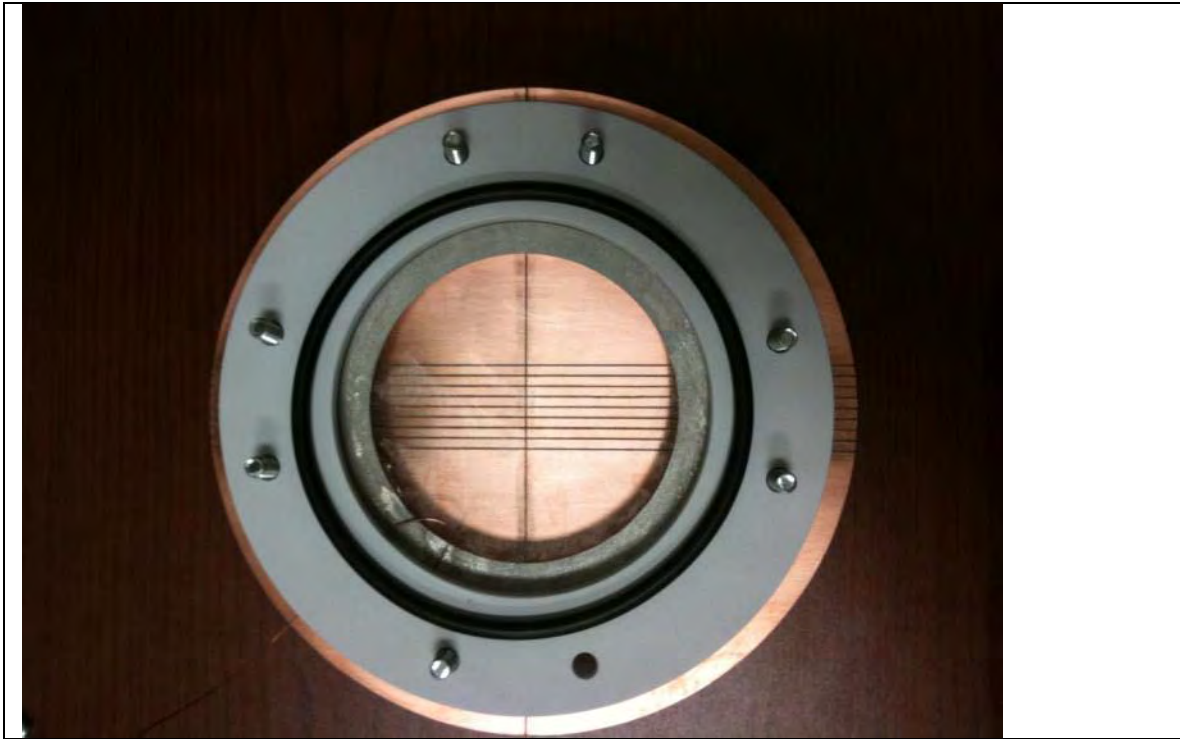
The sequence of pictures below shows the layers in this prototype proceeding from top to bottom. Each picture has one additional layer removed.



1. The top bolt flange keeps pressure on the top ground and cathode layers. This plate is 1/32" double sided G10. The top side is a ground shield and the lower side is the top cathode.



2. Top G10 ground plane.



3. Gas inlet ring and o-ring seal. This version has a gas inlet ring which eliminates positive charge buildup on the gas tubes caused by having the gas feeds enter at the top of the chamber. Eventually the charge buildup leads to a corona discharge to the cathode or ground. The gas inlet holes are on the sides and not visible in this view.



4. Screen ring. The screen now has a machined guard ring to prevent corona at the edges of the screen where there are 14 micron wire tips that have to be terminated in a smooth surface. The stainless screen is soldered to the copper guard ring. The removable screen assembly sits in a groove in the ring.



5. Separator layer used to adjust the screen to cathode distance and the segmented cathode layer. The cathode layer has ten segments on the right (2 guard regions and 8 strips) and ten segments on the left. The left right arrangement will allow us to measure beam centering and jitter and the strips will allow us to test the position resolution of the cathode. The strip pitch is 3 strips per centimeter so we estimate the resolution to be better than a tenth of a millimeter. The serial readout will have a time resolution of about 200kHz per segment giving a complete readout every 100 microseconds.



6. Side view (unassembled). The layers are:

- Top flange
- Top cathode
- Gas feed ring
- Screen layer
- Spacer
- Segmented cathode
- Bottom flange

The Poisson solver software *Poisson Superfish* was used to obtain plots of the field strength, given the detector geometry and potentials. Figure II-8 shows the high field in the vicinity of the micromesh, where signal amplification will occur. Figure II-16 plots the field strength along the central axis of the detector. The signal gain in the detector is related to the field strength.

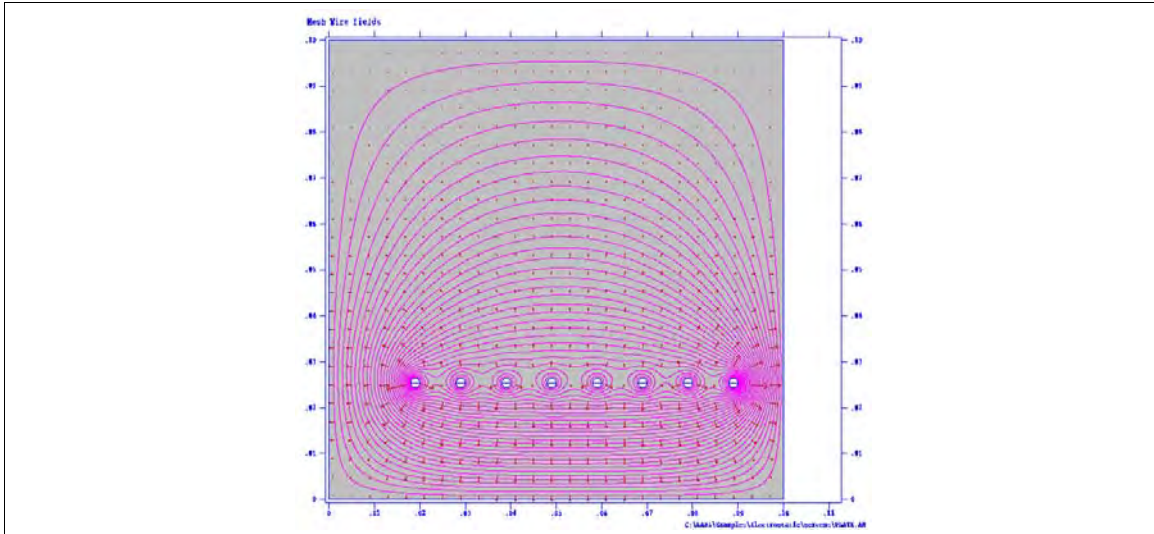


Figure BII-8. Electromagnetic field line plot obtained with the Poisson Superfish software using the prototype detector geometry. The mesh is 12 μm wires at 0.025 cm above the anode. The signal amplification is highest near the micromesh, where the field lines are most dense. Additional amplification is achieved in the amplification gap.

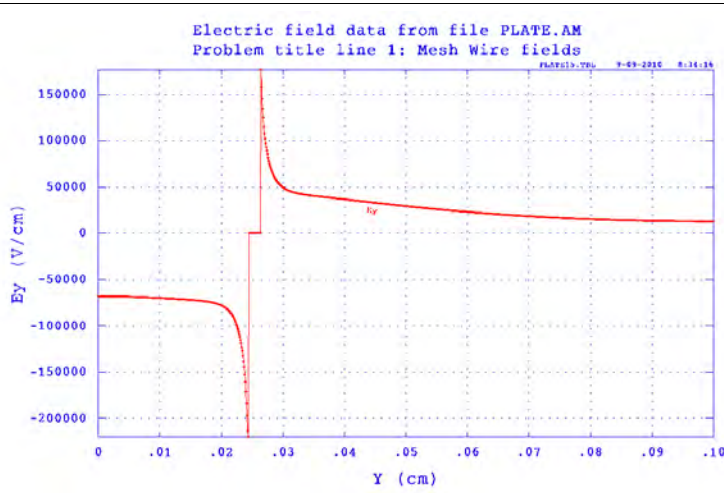


Figure BII-9. Field strength along the central axis from Poisson Superfish (see Figure II-15) showing the high field in the vicinity of the micromesh at 0.025 cm.

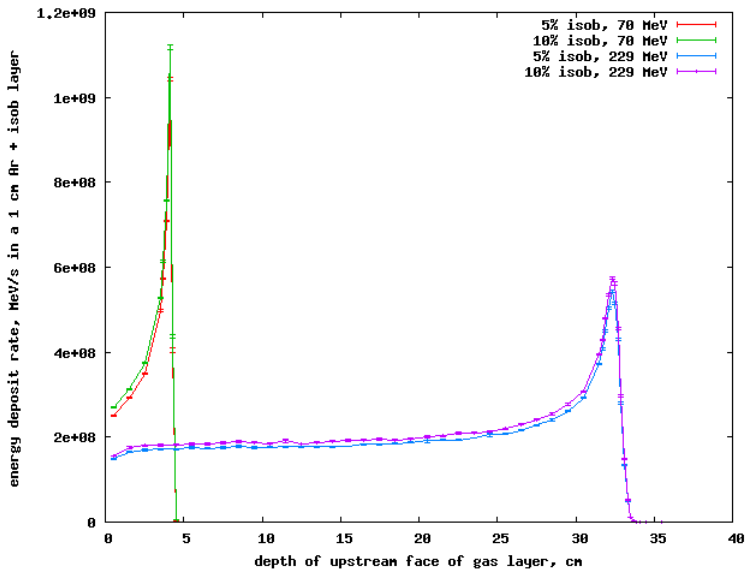


Figure BII-10. Energy deposit in the detector for different gas mixtures from Geant4 Monte Carlo simulation. The gas pressure is 1 atm. The beam current is assumed to be 3 nA, which is typical for double-scattering and scanned pencil beam deliveries.

We will develop this Micromegas design very actively over the next year. We are working with CERN to obtain two small Micromegas prototypes. These prototypes will have narrow amplification gaps, allowing higher field strength and gas gain. The CERN group are the experts in manufacturing Micromegas layers in bulk. We will measure depth dose curves and beam profiles with the 2D layers. Our goal by the end of May 2012 is to have a system of 4 Micromegas layers of at least 20 cm x 20 cm transverse size that can measure a 20 cm x 20 cm x 4 cm segment of any dose distribution (generated with Eclipse or other planning system).

C. Image-Guided and Adaptive Proton Radiotherapy

At this time, we have requested a no-cost extension with a new Scope-of-Work to perform this adaptive study. We are still waiting for a response to this request.

Key Research Accomplishments

The major accomplishment of the past year has been the successful testing of the multileaf collimator. While there is still one component to be delivered and more testing to be performed it is clear that the MLC will be a more efficient method to collimate the proton beam for the majority of fields than using a machined aperture.

A second accomplishment has been the robust growth in clinical treatment protocols for our patients. There are currently 15 IRB-approved proton therapy protocols accruing patients at our center. A total of 189 adults and 44 CHOP patients have completed proton treatment as planned. The total number of completed individual proton treatments is 233. At present, on treatment there are 48 adults and 9 CHOP patients for a total of 57 patients.

Reportable Outcomes

The following abstracts based on work performed on this project have been accepted during the past year at scientific meetings:

1. Optimizing Monte Carlo Parameters to fit Proton-beam Measurements with a Tungsten MLC, PTCOG 2011
2. Monte Carlo Studies of Double Scattering Proton Beam Characteristics with an MLC, DVAAPM Young Investigator Symposium

Conclusions

This report documents the work that has been accomplished during the sixth year of the project to design an MLC for proton radiotherapy, the fifth year of work on the scanned beam project, and the fourth year of work on the image-guided proton therapy project. It concentrates on the past quarter since reports on the other quarters already have detailed those efforts.

